Nicolaus Copernicus University in Toruń

Faculty of Physics, Astronomy and Informatics

Institute of Physics

Department of Atomic, Molecular and Optical Physics

HIGH-RESOLUTION SPECTROSCOPY OF THE 6^{th} OVERTONE BAND OF CARBON MONOXIDE

ALEKSANDR ANDREEVICH BALASHOV

A DISSERTATION

in partial fulfillment of the requirements for the degree of

Doctor of Natural Sciences

in Physical Sciences

Supervisor of Dissertation

dr hab. Katarzyna Bielska

Co-supervisor of Dissertation

prof. dr hab. Daniel Lisak

Toruń June 18, 2023

The research presented in this dissertation was performed within project no. 2018/30/E/ST2/00864 of the National Science Centre, Poland, entitled “High precision and accuracy spectroscopy of weak molecular lines of atmospheric gases”.

Acknowledgements

I would like to express my deepest gratitude to my primary supervisor, Katarzyna Bielska, for her unwavering support, guidance, and mentorship throughout my Ph.D. journey. Katarzyna has not only been an exceptional scientific advisor but also a source of immense encouragement during both professional and personal challenges. She consistently stood by my side, advocating for my success on every step of the way. Her selflessness and commitment to my development as a scientist have left a lasting impact on me. I am truly fortunate to have had Katarzyna as my supervisor and mentor. I cannot express enough appreciation for her dedication and the profound impact she has had on my academic and personal growth.

I extend my sincere appreciation to my additional supervisor, Daniel Lisak, for his contributions to my scientific growth. Daniel's guidance have been instrumental in shaping my research and pushing its boundaries. I am grateful for his support and for sharing his wealth of knowledge with me. I would like to thank him for his valuable expertise and assistance which have greatly enhanced my current scientific knowledge and future career opportunities.

I would also like to express my gratitude to the entire lab team, especially Szymon Wóitewicz and Jolanta Domysławszka, for welcoming me into their exceptional community of experimenters. Working alongside such dedicated and talented people has been a privilege and I am grateful for the opportunity to contribute to cutting-edge science in their company. The collaborative environment and collective efforts have made my research experience immensely fulfilling.

A special acknowledgment goes to Roman Ciuriło for his invaluable insights into the theoretical aspects of my work. Roman's expertise and patience played a crucial

role in expanding my understanding of this challenging domain. I am truly grateful for his support and mentorship throughout my research journey. His knowledge and thoughtful discussions have played a vital role in shaping the direction and depth of my work.

I would also like to extend my heartfelt gratitude to Mikhail Yu. Tretyakov for the opportunities he has provided me to excel in my scientific pursuits and for his tremendous contributions to my scientific vision. His continued communication and interest in my work, along with his role in maintaining connections with my home laboratory in Nizhny Novgorod, have been tremendously helpful and have fostered a sense of belonging throughout my Ph.D. journey.

I am indebted to Oleg Polyanski for creating the opportunity for me to join this project. His belief in my abilities and his support throughout the application process have been pivotal in shaping my scientific journey.

I would like to extend my thanks to Dung Tran, the Postdoctoral Fellow for joining me during his time in the lab. His companionship and friendship outside of work have made my time in the lab more enjoyable.

I cannot overstate the importance of my parents, Natal'ya and Andrey Balashovy, in my life and academic pursuits. Their unconditional love, constant support, and steadfast belief in me have been my pillars of strength. I am forever grateful for their unwavering dedication and encouragement throughout all my goals. I deeply appreciate the countless ways they have contributed to my success and wellbeing, even from afar.

Lastly, but certainly not least, I would like to express my heartfelt gratitude to my best friends, Kiril, Bkmz, and Yogurt. Their support, companionship, and ability to

bring joy into my life during the most challenging times have been invaluable. I am grateful for their camaraderie and providing a much-needed respite from the academic pressures, and for helping me maintain my sanity throughout all this time.

To all those mentioned and countless others who have supported me along the way, I offer my deepest appreciation. This thesis would not have been possible without your support, encouragement, and belief in me. Thank you all for being an integral part of this journey.

Abstract

Carbon monoxide is an important trace gas in the Earth's atmosphere and it is the second most abundant molecule in space. As a relatively simple diatomic molecule, CO is widely used in academic studies, and it serves as a benchmark molecule for testing the most advanced *ab initio* calculations of molecular properties. Advancements in modeling spectra in low-overtone bands of carbon monoxide revealed that further improvement required experimental studies of 6^{th} overtone of CO because calculations involving highly excited molecular states are very sensitive to the small changes in the physical model as well as to the precision of numerical calculations. In this work the results of an experimental study of never before measured 6^{th} overtone band of carbon monoxide near 690 nm are presented. Improvement of the cavity ring-down spectrometer allowed measurement of 14 transitions from $(7-0)$ band with intensities below $2{\cdot}10^{-29}$ cm/molecule. Line intensities are determined with relative standard uncertainty below 4% and line positions with an accuracy of $3 \cdot 10^{-4}$ cm^{-1}. Self-induced pressure broadening and shifting coefficients are determined with a relative uncertainty of about 5%. Speed-dependent line-shape effects are observed and analyzed for the first time for such weak transitions.

The high accuracy of measured line intensities motivated new *ab initio* calculations done by collaborators from the University College London, UK, with the aim of developing a model of CO absorption capable to predict line intensities of all bands within the experimental uncertainty. The validation of new calculations with the experimental data allowed to find and overcome issues with initially huge errors and resulted in a model that predicts the measured values of 6^{th} overtone line intensities within the experimental uncertainty of a few percent, which is an important step towards a single model predicting the entire CO spectrum.

Streszczenie

Tlenek węgla występuje w śladowych ilościach w atmosferze ziemskiej i jest drugą najbardziej rozpowszechnioną cząsteczką w przestrzeni kosmicznej. Jako stosunkowo prosta cząsteczka dwuatomowa, CO jest szeroko stosowany w badaniach akademickich i służy jako cząsteczka wzorcowa do testowania najbardziej zaawansowanych obliczeń *ab initio* własności cząsteczek. Postępy w modelowaniu pasm absorpcyjnych tlenku węgla, tzw. niskich nadtonowów ujawniły, że dalsza poprawa wymaga pomiarów szóstego nadtonu CO. Wynika to z faktu, iż obliczenia dla silnie wzbudzonych stanów są bardzo czułe na małe zmiany w modelu fizycznym jak również precyzję obliczeń numerycznych. W pracy przedstawiono wyniki badań eksperymentalnych nigdy wcześniej nie mierzonego pasma $(7-0)$ tlenku węgla w zakresie długości fali około 690 nm. Udoskonalenie spektrometru strat we wnęce (CRDS, ang. *cavity ring-down spectrometer*) umożliwiło pomiar 14 przejść z tego pasma o natężeniach linii poniżej $2{\cdot}10^{-29}$ cm/molekuła. Natężenia linii zostały wyznaczone z względną niepewnością standardową poniżej 4%, a położenia linii z dokładnością $3 \cdot 10^{-4}$ cm^{-1}. Współczynniki zderzeniowego rozszerzenia i przesunięcia linii są wyznaczone z względną niepewnością około 5%. Po raz pierwszy dla tak słabych linii zostały zaobserwowane efekty zależności rozszerzenia i przesunięcia linii od prędkości absorbera i wyznaczone wartości charakteryzujących je parametrów.

Wysoka dokładność zmierzonych natężeń linii była motywacją dla nowych obliczeń *ab initio* wykonanych przez współpracowników z University College London (Wielka Brytania). Walidacja nowych obliczeń przy pomocy danych eksperymentalnych pozwoliła znaleźć i przezwyciężyć problemy powodujące początkowo bardzo duże rozbieżności między teorią i doświadczeniem. Zaowocowała ona modelem, który przewiduje wartości natężeń linii z szóstego nadtonu CO zgodne z wartościami uzyskanymi w pomiarach.

Jest to istotny krok na drodze do uzyskania jednego modelu, który przewidywałby natężenia linii widmowych CO w paśmie podstawowym oraz wszystkich nadtonach.

TABLE OF CONTENTS

Notations and Abbreviations

A | C | D | E | F | G | H | I | M | N | O | P | Q | R | S | U | V

A

ADC analog to digital converter. 30

AOM acousto-optic modulator. 21, 25, 26, 28–30

C

CMDS Cavity Mode Dispersion Spectroscopy. 66

CMWS Cavity Mode Width Spectroscopy. 19, 20, 28, 30, 66

CRDS Cavity Ring-Down Spectroscopy. 17, 20, 21, 27, 30, 65, 66

D

DMC dipole moment curve. 15, 16, 61

DN Dickie narrowing. 38, 39, 71

E

ECDL external cavity diode laser. 26, 27

EOM electro-optic modulator. 21, 27, 30

F

FR Faraday rotator. 27

FSR free spectral range. 24, 26, 28

FWHM full width at half-maximum. 20, 26, 36, 37

G

GOSAT Greenhouse Gases Observing Satellite. 12

GP Galatry profile. 39

H

HITRAN high-resolution transmission molecular absorption database. 37, 42, 47, 48, 56, 57, 60–63

HTP Hartmann-Tran profile. 40, 48

HWHM half width at half-maximum. 58, 59

I

IR infrared. 14, 17, 66

IUPAC International Union of Pure and Applied Chemistry. 40

M

MOPITT Measurement of Pollution in the Troposphere. 12, 14

N

Nd:YAG neodymium-doped yttrium aluminum garnet. 24, 26

NGP Nelkin-Ghatak profile. 39

O

OCO Orbiting Carbon Observatory. 12

OFC optical frequency comb. 29, 30

P

PBS polarizing beam splitter. 26, 27

PDH Pound-Drever-Hall. 27, 28

PEC potential energy curve. 15, 16, 61, 62

PI proportional–integral controller. 26

PID proportional–integral-derivative controller. 27

PZT piezo transducer. 24

Q

QF quality-of-the-fit factor. 44, 58, 59

qSDNGP speed-dependent Nelkin-Ghatak profile with quadratic approximation of speed dependence. 39, 40, 48–51, 71

qSDVP speed-dependent Voigt profile with quadratic approximation of speed dependence. 38, 40, 48–51, 53–58, 60, 62–64, 70, 71

QWP quater wave plate. 26

R

RD ring-down. 18–20, 24, 30, 32, 33, 48, 49

RDC ring-down cavity. 21–28, 30, 31

RF radio frequency. 27, 29

RTD resistance temperature detectors. 22, 23

S

SD speed dependence. 37–39, 55, 57

SNR signal-to-noise ratio. 19, 32, 39, 43, 44, 50, 54

U

UCL University College London. 61, 65

UTC Coordinated Universal Time. 29

UV ultraviolet. 14

V

VP Voight profile. 35, 36, 40, 48–50, 55, 57, 60, 64, 70

Introduction

The global goal of this work is to advance our current understanding of the physical world on a molecular level. Various exciting areas of current research include several tests of the fundamental laws of physics. There were done laboratory measurements in search of molecular transitions that violate the symmetrization postulate of quantum mechanics thus setting an upper limit for its potential violation [1, 2]. H_2 lines are used for investigation of potential variations of the proton-to-electron mass ratio both in laboratory experiments [3] and on the cosmological scale in the absorption spectra of quasars [4]. Comparable experimental methods are utilized to explore the possibility of a cosmological variation of the electromagnetic fine structure constant [5]. Additionally, after redefining the Kelvin unit in 2019 , molecular spectroscopy was proposed [6] as a tool for primary linestrength ratio thermometry (LRT). It can achieve ppm-level (parts-per-million) accuracy for CO optical transitions (80–700 K) and rare-earth-doped crystals (9–100 K).

Another application of molecular spectroscopy is the remote sensing of gases. It can provide comprehensive information about the composition and conditions of the Earth's atmosphere, interstellar media, stars, exoplanets, molecular clouds, and other space objects. The carbon-to-oxygen ratio measurements provide information on the history of the formation of exoplanets [7]. Numerous satellite missions, as well as ground-based laboratories, target remote sensing of the Earth's atmosphere allowing a wide range of measurements: the Measurement of Pollution in the Troposphere (MOPITT) [8], the Orbiting Carbon Observatory (OCO)-2 and -3 [9, 10], and the Greenhouse Gases Observing Satellite (GOSAT) [11] and GOSAT-2 [12] missions were deployed for advanced monitoring of greenhouse gases. Several thermal enhanced infrared sounders such as AIRS [13], TES [14], IASI [15], and CrIS [16] were launched

to monitor the atmospheric state for numerical weather prediction and climate change. They provide measurements of atmospheric temperature profiles, humidity profiles as well as vertical profiles of important pollutants and greenhouse gases such as carbon monoxide, ozone, methane, and SO_2. In addition to these more traditional passive observations, active measurements like the CloudSat lidar [17] and the CALIPSO radar [18] satellites were deployed for monitoring the vertical structure of clouds and aerosols that are important for diverse atmospheric applications.

Closing on the applications targeted by the findings in this thesis, let us mention that a deeper understanding of processes of intermolecular interactions is essential for the development of small molecule machines [19]. The study of van der Waals interactions can significantly impact the development of lithium solid polymer electrolytes [20], which are considered to be promising alternatives to their widely used liquid counterparts and engineering "graphene-on-surface" structures for applications including optoelectronics, surface catalysis, anti-friction, and superlubricity [21].

For the success of all aforementioned applications, there must be a complete and comprehensive understanding of the object used in applications, meaning there should be its physically justified theoretical model. Quantum mechanical calculations for systems larger than hydrogen, though would describe completely observed spectra seem not feasible for the current level of computational abilities. That is why different approximate methods are used for calculating spectra. Such calculations that provide the required level of accuracy for every particular case of interacting molecules or even conditions of the gas are considered as a distinguished result. Experimental laboratory measurements provide necessary validation for the calculations because they allow for high resolution and accuracy, tight control over measurement conditions, sample composition, and isolation of particular effects of interest. Simple molecu-

lar systems are preferable for this task since quantum mechanics calculation requires huge computational power for large molecules.

For this reason, carbon monoxide might be the best object for the study. It is a simple diatomic molecule with a strong electric dipole moment. Over the long history of molecular spectroscopy, CO became a benchmark system for the study of rotational and rotational-vibrational transitions and has been presented in many textbooks. Carbon monoxide is widely used in the study of astrophysical environments, because beyond Earth it is the second-most common diatomic molecule in the interstellar medium, after molecular hydrogen. The molecular hydrogen spectrum in the infrared (IR) region is much weaker than that of CO because H_2 is a symmetric molecule having no dipole moment. While molecular hydrogen is usually observed only in the ultraviolet (UV) range, thus requires the use of space telescopes, carbon monoxide observations, which can be done from the Earth, provide information about the molecular clouds [22, 23], in which most stars form. CO is also present in the atmospheres of Venus [24, 25], Mars [26], and exoplanets [27, 28]. Carbon monoxide is one of the symptomatic gases used in disease diagnostics based on breath analysis [29]. It is one of the major trace gases in Earth's atmosphere as well [30]. It does not have a direct effect on the global temperature but plays an important role in atmospheric chemistry [31]. It is a pollutant in the terrestrial atmosphere (especially in the troposphere), occurring from both natural (i.e., biomass burning) and anthropogenic (fossil fuel combustion) sources. It is formed by the reaction of the OH radical with volatile organic compounds. Furthermore, the oxidation of CO by OH results in the formation of ozone and CO_2. Carbon monoxide is routinely monitored using different spectrometers onboard remote-sensing satellites, including MOPITT [8], ACE [32], and TROPOMI [33].

In this thesis, the following notation for the vibrational bands of the CO molecule is used: $(\mathsf{v}'' - \mathsf{v}')$, where v'' − vibrational quantum number of the upper level of the transition, and v' − of the lower one. The $(1-0)$ band is called fundamental, and the bands with $\mathsf{v}' = 0$, and $\mathsf{v}'' > 1$ − are overtones. Thus, the band $(7-0)$ is often referred to as the sixth overtone. Bands with $\mathsf{v}' > 0$ are called hot bands. Further, the notation of rotational transitions accepted in spectroscopy is used: P denotes transitions from a state with a rotational quantum number J'' to a state with J', when $\Delta J = J' - J'' = -1$, R denotes transitions with $\Delta J = 1$ and Q with $\Delta J = 0$. It is also often convenient to introduce the quantum number m, where $m = -J''$ for the P-branch and $m = J'' + 1$ for the R branch.

From the theoretical point of view calculations of CO line intensities are relatively simple due to the simplicity of the molecule. However, for high vibrational number overtones, the calculation becomes more and more sensitive to changes of potential energy curve (PEC) and dipole moment curve (DMC) because of increasing density of molecular levels and increasing effects of non-rigidity of the molecule. The experimental data on highly excited overtones are sparse since the intensity of each successive overtone drops roughly two orders of magnitude with increasing the vibrational number by one, thus making it increasingly difficult to detect higher CO overtones using absorption methods. Nonetheless, highly exited states manifest themselves at high temperatures and are important for studies of solar and stellar atmospheres as well as combustion processes on Earth. High vibrational overtones find applications in fundamental research as they are sensitive to the proton-to-electron mass ratio [34]. Hot bands of high vibronic states of CO were observed in stellar spectra [35–40] which helps study the processes of star formation. It took more than four decades from the first measurements of emission hot bands up to $(7-5)$ in an acetylene flame

[41] in 1974 until the first measurement of the $(6-0)$ overtone band [42].

This work is devoted to the first measurements of $(7-0)$ overtone transitions. The rotational distributions of intensities in the fundamental $(1-0)$ and low-overtone ($(2-0)$ and $(3-0)$) vibrational bands of carbon monoxide are nearly immune to the changes of the form of the PECs and DMCs [43]. Contrary, for high-$\Delta\mathsf{v}$ overtones (where v is a vibrational quantum number), Medvedev et al. [43] showed that line intensities are very sensitive to different approaches of calculating the dipole moment curves. So in order to properly model CO absorption such a model needed to be verified with the highest possible overtone measurement, where it is most sensitive. This situation showed the need for experimental study of 6^{th} overtone unequivocally indicated by Meshkov et al. [44].

CHAPTER 1

Measurement technique

The predicted values of the transitions from 6^{th} overtone of CO were ranging from 1 to 5 cm/molecule times 10^{-30} [45], and the goal was to not only register expected transitions but also to provide quantitative information about values of intensities and line-shape parameters. This narrows available experimental techniques to cavity-enhanced ones. One of the most popular and well-known techniques of absorption determination with an optical cavity is Cavity Ring-Down Spectroscopy (CRDS). It was proposed in IR range in 1988 [46]. The CRDS was already shown to be capable of achieving measured line intensities as low as $1.5 \cdot 10^{-31}$ cm/molecule, which was shown on the example of nitrogen electric quadrupole transitions [47].

1.1. CRDS

Let's consider an optical cavity, formed by two mirrors, with reflectivity R separated by the distance l. At the first step, the radiation is injected into the cavity. The light inside the cavity reflects back and forth many times. If the frequency of radiation is so that the whole number of half-periods fit between the mirrors, i.e. the radiation is in resonance with the cavity, then light inside the cavity constructively interferes, building up the intensity. Then at some arbitrarily chosen intensity level, the radiation pumping is stopped. If only one cavity mode is exited, then the intensity of the radiation inside the cavity on every pass is attenuated by the reflection from the mirror, and absorption in the medium between the mirrors according to the Beer-Lambert law:

$$R \cdot e^{(-\alpha \cdot l)}, \tag{1.1}$$

where α is absorption coefficient.

After N reflections the intensity inside the cavity is given by:

$$I(\mathrm{N}) = I_0 \cdot \left(R \cdot e^{(-\alpha \cdot l)}\right)^{\mathrm{N}} \tag{1.2}$$

where $I(\mathrm{N})$ is the radiation intensity inside the cavity and I_0 – initial intensity. Rewriting expression 1.2 with R in the exponent and number of reflections N as $\frac{c \cdot t}{n \cdot l}$, where c is the speed of light in vacuum and n is the refractive index of the medium inside the cavity, it changes to:

$$I(t) = I_0 \cdot e^{(\ln(R) - \alpha \cdot l)\frac{c \cdot t}{n \cdot l}}, \tag{1.3}$$

or simply:

$$I(t) = I_0 \cdot e^{-\frac{t}{\tau_{\mathrm{RD}}}}, \tag{1.4}$$

where τ_{RD} is a time at which the intensity decreases by e times called the ring-down (RD) decay time constant:

$$\tau_{\mathrm{RD}} = \frac{n \cdot l}{c} \cdot \left(\frac{1}{-\ln(R) + \alpha \cdot l}\right), \tag{1.5}$$

For high reflectivity mirrors $(1 - R \ll 1)$ taking the first term of the Tailor series of logarithm function near unity, the last expression can be rewritten as

$$\tau_{\mathrm{RD}} = \frac{n}{c} \cdot \frac{l}{(1 - R) + \alpha \cdot l}. \tag{1.6}$$

Signal leaking through the cavity mirror, being proportional to the light intensity inside the cavity, will decay at the same rate. Approximating measured signal with a

function 1.4 allows to determine the RD time constant. The total losses in the cavity are then composed of the losses due to sample absorption and self-losses:

$$\alpha = \frac{n}{c} \cdot \left(\frac{1}{\tau_{\mathrm{RD}}} - \frac{1}{\tau^{\mathrm{self}}} \right), \text{ where } \tau^{\mathrm{self}} = \frac{n}{c} \cdot \frac{l}{(1-R)+X}, \tag{1.7}$$

where X represents other miscellaneous optical losses such as diffraction losses and losses due to scattering by the medium that includes in the self-losses. For simplicity, X has been omitted in the above derivation.

In theory, self-losses of the cavity can be measured with empty or filled with a non-absorbing gas cavity, however, in practice, it is quite a difficult task to do, especially in high signal-to-noise ratio (SNR) measurements. The self-losses of the cavity can be accounted for mathematically by properly choosing the model of the absorption and self-losses observed as a sample spectrum background and fitting them to the data.

The single RD measurement happens on a sub-millisecond time scale, much faster compared to the following technique. This allows for averaging more measurements per frequency, and thus lowering the noise.

1.2. CMWS

The Cavity Mode Width Spectroscopy (CMWS) [48, 49] technique is based on the determination of losses in the cavity by measurement of the width of cavity response. The frequency of the radiation source is scanned near the cavity resonance frequency, and the response shape is recorded. Further approximation of acquired response by Lorentz function yields a determination of the mode width, which is related to the total cavity losses:

$$\Lambda^{\mathrm{tot}} = \frac{c}{2\pi n l} \cdot \left((1-R) + X + \alpha \cdot l \right), \tag{1.8}$$

where Λ is the mode full width at half-maximum (FWHM). Similarly, as with measurements of the RD time, determining absolute absorption in gas inside the cavity requires accounting for self-losses:

$$\alpha = \frac{2\pi n}{c}\left(\Lambda^{\text{tot}} - \Lambda^{\text{self}}\right), \text{ where } \Lambda^{\text{self}} = \frac{c}{2\pi n l} \cdot \left((1-R) + X\right). \tag{1.9}$$

where Λ^{tot} is the total mode width FWHM, and Λ^{self} represents the width related to the self-losses.

In this work for measurement of the 6^{th} overtone of CO was used only CRDS technique as it is much more sensitive to low absorption than CMWS. CMWS technique has the advantage of a wider dynamic range of absorption measurement and was used in a testing phase to estimate the nonlinearity of the detection system that is described in chapter 2.4.

CHAPTER 2

Experimental setup

Aside from the extremely low intensities of CO $(7-0)$ band transitions, another practical challenge was the spectral range of the measurement. Crucial components such as acousto-optic modulators (AOMs) and electro-optic modulators (EOMs) as well as broadly tunable lasers were not as commonly available as for the telecommunication range (1200 − 1600 nm) where such weak lines were measured [47, 50]. The experimental group in Torun specialized in CRDS technique and has already shown [51] the possibility to build a CRDS setup working in the visible range.

The measurement setup is a rebuilt version of the cavity ring-down spectrometer used in Ref. [52] (and references therein). For this work, it required modifications in order to measure extremely weak transitions. It was necessary to decrease the noise level to improve the sensitivity of the measurement.

2.1. Absorption cell

The absorption cell is made from an 1/4 inch stainless steel tube with a bellow at the center that is held by two angled plates having a thickness of 30 mm connected with four invar rods 20 mm in diameter. The ring-down cavity (RDC) was rebuilt to incorporate angled windows to reduce unwanted reflections from them. The cell is placed inside a thermally insulated enclosure made from extruded polystyrene foam with an acrylic sheet at the bottom and secured on the optical table with plastic screws to minimize heat transfer. The thermal enclosure is not sealed hermetically and has holes on both sides to pass through the laser beams. The temperature inside is stabilized with six Peltier elements incorporated in the ceiling of the enclosure

connected in series. They are placed in a row along the RDC and operate in a heating or cooling regime when necessary. Aluminum radiators with fans on both sides of Peltier elements allow for better heat transfer. Because of non-ideal thermal insulation and different efficiency of Peltier elements due to manufacturing tolerances a small natural temperature gradient can occur along the RDC.

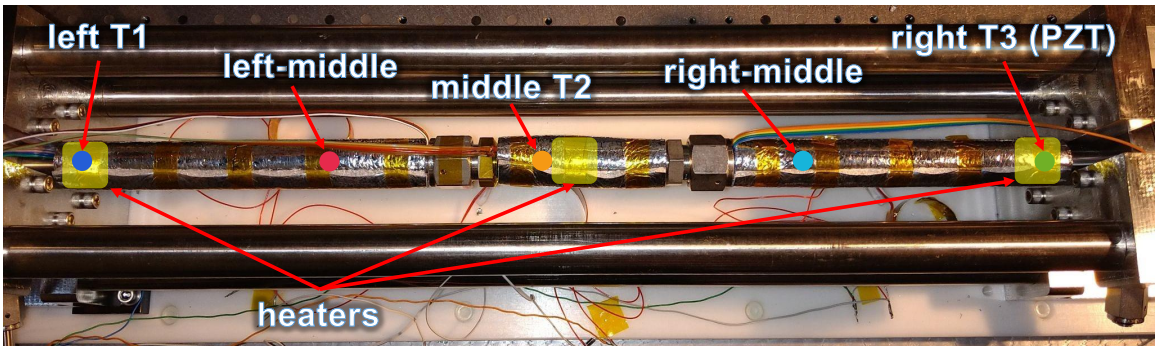

Figure 2.1: Five pt100 temperature sensors are placed along the cavity for temperature measurement. Three resistive heaters near resistance temperature detectorss (RTDs) T1, T2, and T3 are used for active gradient equalization.

Four small fans inside the thermal insulation help to circulate the air inside to minimize the temperature gradient. Additionally, three small resistive heaters (one in the center and two at the sides) are wrapped around the cell to actively equilibrate the temperature gradient. Temperature measurement is done with pt100 RTD. Five RTDs are equally spaced along the measurement cell and one reference Fluke type 5641 thermometer is placed close to one of them. Figure 2.1 shows the placement of temperature sensors and heaters for the gradient equalization. Temperature stabilization is implemented with a custom proportional–integral controller, programmed in Labview, that stabilizes the central RTD (T2) to the set temperature by controlling the current through the Peltier elements. Once the temperature is stable the active gradient equalization begins: the program turns on two of three additional heaters to bring the temperature of two coldest from three RTDs (the most left (T1), mid-

dle (T2) and most right (T3)) to the temperature of the hottest one. Two RTDs are added between the main three for monitoring the residual temperature gradient. Plot 2.2 shows typical variations of temperature of the RDC during 30 scans of P1 line measurement at 100 Torr. Temperature oscillations correlate with room temperature variation caused by air conditioning systems inside the laboratory.

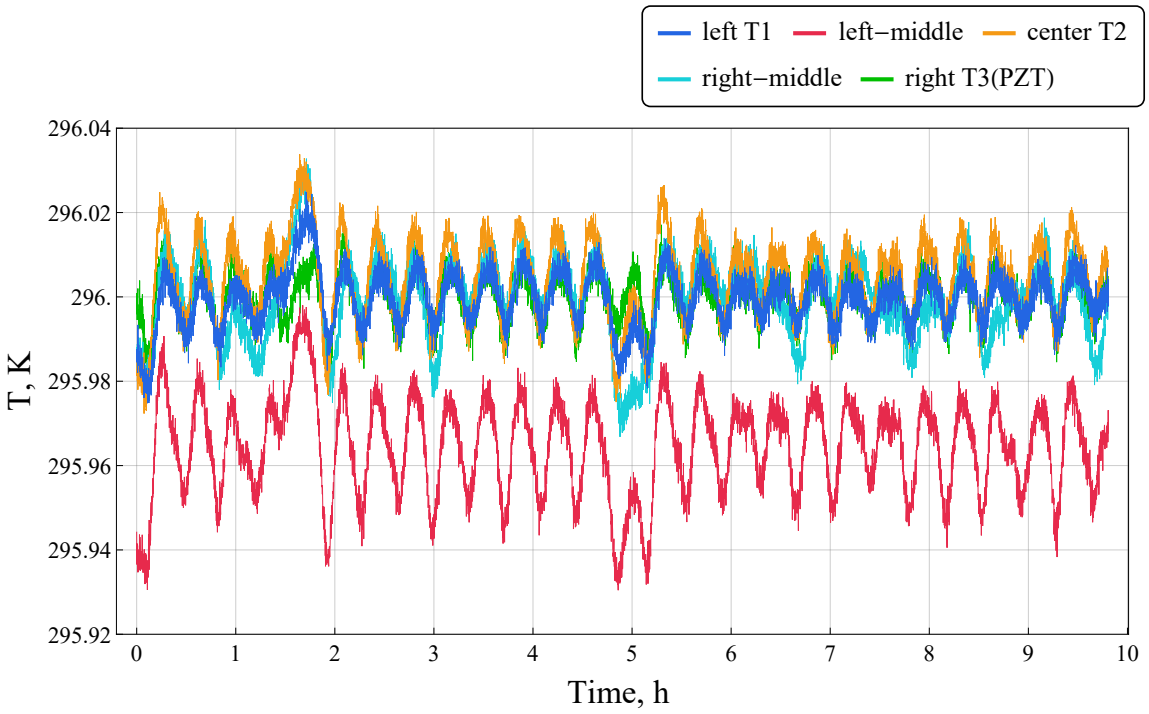

Figure 2.2: Temperature recorded in the center of the cavity, at its sides and at intermediate points for the measurement (30 scans) of P1 line at 100 Torr.

Calibration of RTDs against two factory-calibrated Fluke type 5641 thermometers was done in our laboratory using a copper block inside a thermally insulated box. The Fluke thermometers have 1 mK manufacturer-stated calibration uncertainty and re-calibration after 4 years showed that the long-term drift is below 7 mK. The Peltier element attached to the copper block allows to change the temperature. For calibration, each RTD together with two reference Fluke type 5641 thermistors is placed inside an individual hole in the copper block. Resulted standard uncertainty of tem-

perature reading is within 30 mK. Combining it with 18 mK standard uncertainty of temperature gradient and stability observed during measurements gives 35 mK of the total standard uncertainty of temperature stability in the RDC. The calibration was checked again right after all the measurements of (7-0) overtone was done and confirmed that it is still valid.

Pressure measurement was done with Wika CPG2500 pressure sensor from Mensor. The manufacturer's specified full range (900 Torr) accuracy was 0.08 ‰. After comparison with another factory-calibrated sensor of the same model, the total relative uncertainty of pressure measurement was estimated to 0.13 ‰. This value accounts for experimental conditions in the laboratory, including the temperature variation.

The cavity length of about 74 cm corresponds to free spectral range (FSR) of 203 MHz. The RDC is formed by two spherical dielectric mirrors with double-wavelength coating in a non-confocal configuration. One of the mirrors, mounted on a piezo transducer (PZT)-actuated mount, is used for closed-loop control of the cavity length. The nominal reflectivity of mirrors was 99.9988 % which corresponds to approximately 206 μs of the RD time constant in empty cavity in the $698 - 690$ nm range corresponding to 6^{th} overtone of CO and about 96 % at 1064 nm, corresponding to the reference neodymium-doped yttrium aluminum garnet (Nd:YAG) laser, which is used for stabilization of length of the RDC. The length stabilization system is discussed in more detail below in chapter 2.2.

2.2. Optical setup

The cavity length is stabilized by locking the comb of its eigenfrequencies to the Nd:YAG reference laser, whose frequency is locked to the frequency of the iodine hyperfine line and has long-term stability better than 5 kHz. Fig. 2.3 shows the

principal scheme of the setup, including the cavity length stabilization system.

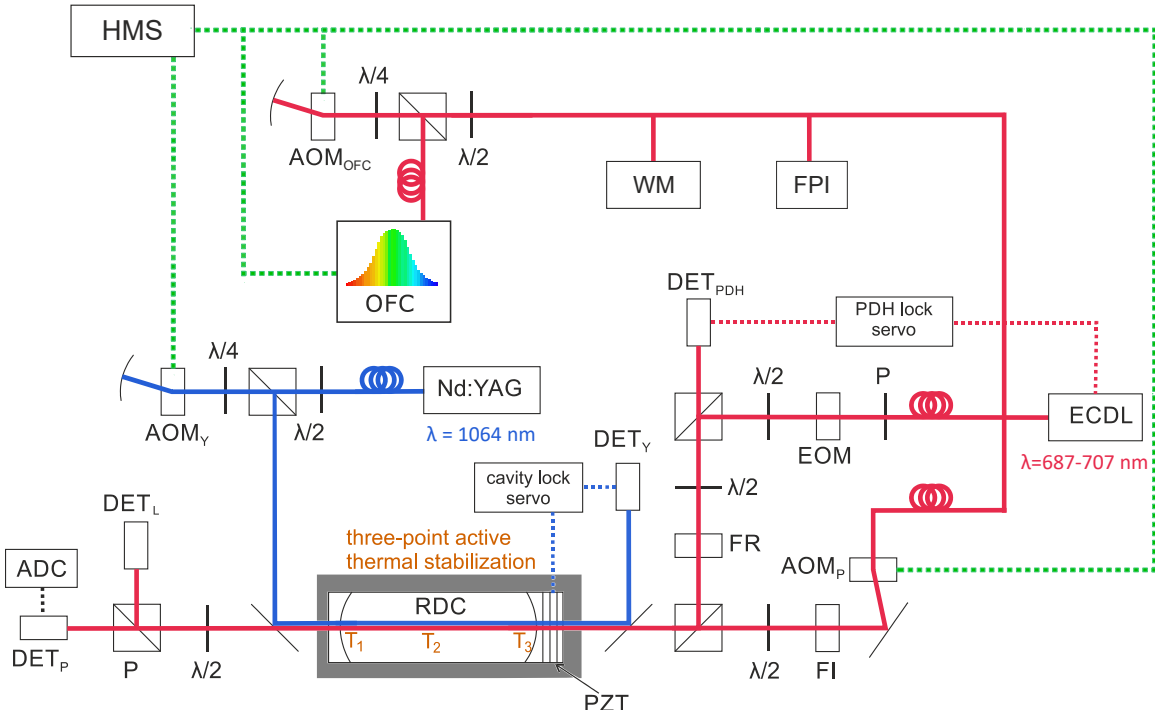

Figure 2.3: Schematic diagram of the spectrometer. ECDL – probe laser, Nd:YAG – iodine stabilized reference laser, OFC – optical frequency comb, HMS – hydrogen maser standard, RDC – ring-down cavity, PZT – piezo transducer, $\mathrm{AOM_Y}$, $\mathrm{AOM_P}$, $\mathrm{AOM_{OFC}}$ – acousto-optic modulators, EOM – electro-optic modulator, $\mathrm{DET_Y}$, $\mathrm{DET_{PDH}}$, $\mathrm{DET_L}$, $\mathrm{DET_P}$ – photodetectors, WM – wavemeter, FPI – Fabry-Perot interferometer, FI – Faraday isolator, FR – Faraday rotator, $\lambda/2$ and $\lambda/4$ – half- and quarter-wave plates accordingly, P – linear polarizer, ADC – analog to digital converter. Blue solid lines indicate Nd:YAG reference beam, red solid lines indicate the probe laser beams, whereas dotted lines mark servo loops and electrical signals.

The reference laser beam frequency is shifted by $2f_{\mathrm{AOM}}$ and modulated at a frequency $f_{\mathrm{mod}} = 50$ kHz with a modulation depth of 2 MHz, which is carried out by a variable-frequency AOM ($\mathrm{AOM_Y}$, figure 2.3) configured in a double-pass arrangement. The modulated reference beam is coupled to the RDC and the transmission signal is detected by New-Focus (Model 2053) photo-detector ($\mathrm{DET_Y}$, figure 2.3). The lock-in amplifier provides the required derivative of the transmission signal after its demod-

ulation with a time constant of 1 ms, which is much longer than $1/f_{\mathrm{mod}}$. It then serves as an error signal that is passed to the proportional–integral controller (PI), connected to the driver for the piezo transducer. The alterations of AOM modulation frequency f_{AOM} change both the frequency and the direction of the reference beam. Therefore, a single-pass setup would make it impossible to maintain beam alignment into the RDC when the reference laser frequency is altered. The optical scheme of AOM double-pass configuration is shown in figure 2.3. The linearly polarized Nd:YAG laser beam passes through a polarizing beam splitter (PBS) and quater wave plate (QWP) ($\lambda/4$) that converts it to circularly polarized light. Subsequently, it is focused inside the AOM crystal that operates near the Bragg condition to ensure that most of the power is diffracted into the first-order component and reflected back by the spherical mirror. The distance between the AOM and the spherical mirror is equal to the radius of curvature of the mirror. The second pass through both the AOM and QWP makes a linearly polarized beam that gets diffracted into the first-order beam that propagates in the same direction as the incident one but has a polarization plane perpendicular to that of the incident beam and they get separated by PBS. This scheme outputs the reference beam shifted by $2f_{\mathrm{AOM}}$ with the direction independent of f_{AOM}. Alternating the f_{AOM} thus frequency of the reference beam allows to tune the cavity length if this change is made slow enough that the lock is able to follow it. Changing the cavity length allows to translate cavity mode frequencies, and thus reduces the measurement step below the FSR, similarly as in Ref. [53]. The region near the line center (about 3 FWHM of the absorption line width) was measured with a frequency step of about 50 MHz, while line wings were recorded with one FSR frequency step.

The radiation source for the visible range was an external cavity diode laser (ECDL)

(Toptica DL Pro) from Toptica Photonics with a wavelength range from 687 to 707 nm. The laser beam was divided into several beams. Two main beams with orthogonal polarisations were coupled to the RDC. One of them was used to lock the laser frequency to the frequency of cavity mode (locking beam) with Pound-Drever-Hall (PDH) technique [54, 55]. This also allows us to actively narrow the probe laser line width from about 100 kHz to two orders of magnitude lower than the one of the RDC. The PDH technique is described in detail in the paper [56] and the application of the PDH technique to a CRDS system was also explained in Ref. [57].

The use of the EOM driven by $\Omega = 20$ MHz radio frequency (RF) signal for phase modulation of the lock beam creates side bands on combination frequencies required for PDH locking. The amplitude of the EOM modulation is chosen so that only the first order pair of anti-phase sidebands are generated with a sideband-to-carrier intensity ratio of about 1:10. A linearly polarized locking beam passes through the EOM, a PBS, and a Faraday rotator (FR) before being directed into the RDC. The radiation reflected from the front cavity mirror consists of light from the two sidebands (which are totally reflected from the cavity) and a fraction of the incident light at the optical carrier frequency. This radiation propagates back through the FR and is directed to the 125 MHz bandwidth photoreceiver (New Focus, Model: 1801) denoted in figure 2.3 as $\mathrm{DET_{PDH}}$ to create a beat note with the beam leaking from the cavity giving, after demodulation, a sharp error signal for the frequency stabilization of the ECDL. This error signal filtered by fast proportional–integral-derivative controller (PID) (Toptica FALC) controls the laser diode current to stabilize its frequency to the central frequency of RDC mode.

The second beam was used as the probing beam for the spectroscopic measurement. Inside the cavity, it has polarisation orthogonal to the locking beam and also frequency

shifted by one FSR by means of AOM, marked AOM_P on the figure 2.3. The AOM_P has a tuning range that allows it to shift the frequency of the probe beam over the entire range of the cavity mode. This enables the measurement of the position of the mode and fine-tuning of the probe beam frequency to achieve maximal transmission through the cavity. It also allows for measurement of the mode width for the CMWS technique. Precise tuning of the probe beam to the center of the cavity resonance, and sufficiently high extinction ratio of its power (significantly more than 58 dB, although the exact value is too high to be measured), ensures that the determination of the time constant required for calculating sample absorption is not affected by any systematic errors that may arise from interference between incompletely switched-off pumping beam and the decaying beam inside the RDC [58].

The experimental setup incorporates additional beams. One beam facilitates the monitoring of single-mode laser operation via a Fabry-Pérot interferometer (FPI). It was used to check the single-mode operation of the laser in the required spectral range before each measurement. It is required to maintain the single-mode operation of the laser because otherwise PDH locking of the laser's frequency would be lost or the laser would lock on the wrong frequency. Another beam was used for rough optical frequency measurements, using a wavemeter (WM) to ascertain the comb tooth number.

In the course of preparations for the measurements described in this thesis, crucial optical elements such as lenses that couple laser beams to the RDC were mounted on shorter, more sturdy posts as well as the cavity itself brought down − closer to the optical table to increase mechanical stability.

2.3. Frequency measurement

To obtain precise optical frequency measurements across a given spectrum, an optical beat note is generated between the probe laser beam and the optical frequency comb (OFC). The laser beam's frequency is deliberately shifted using a $\mathrm{AOM_{OFC}}$ in double-pass configuration to match the beat note detection system's bandwidth. The frequency of the laser ν_L is calculated by:

$$\nu_\mathrm{L} = f_0 + m \cdot f_\mathrm{rep} + f_\mathrm{beat} - 2 \cdot f_{\mathrm{AOM_{OFC}}}, \tag{2.1}$$

where f_0 is the carrier-envelope offset frequency of the OFC, f_rep is it's the repetition frequency, f_beat is the frequency of the beat note between m-th tooth of the OFC and frequency of the laser shifted by 2 $f_{\mathrm{AOM_{OFC}}}$, which is modulation frequency of the $\mathrm{AOM_{OFC}}$ (figure 2.3), and m in the comb tooth number that is calculated from rough measurement of ν_L with the wavemeter (WM, figure 2.3):

$$d = \mathrm{Round}\left(\frac{\nu_\mathrm{WM} \mp f_0 \mp f_\mathrm{beat}}{f_\mathrm{rep}}\right), \tag{2.2}$$

where ν_WM is the laser frequency measured with wavemeter. The accuracy of the wavemeter of about 60 MHz was sufficient because the distance between consecutive teeth of the OFC f_rep was approximately 250 MHz. The spectrometer's frequency counters, signal generators (including AOM drivers), and OFC are synchronized to a 10 MHz RF signal [59] that originates from a hydrogen maser [60]. This signal acts as a reference point to Coordinated Universal Time (UTC) and is transmitted to our laboratory through a fiber link [61, 62] from the Astro-Geodynamic Observatory (AOS) in Borowiec, Poland. The 10 MHz signal has stability of $2{\cdot}10^{-13}$ at 1 s [59].

2.4. Tests of the ring-down time measurements

Before the measurement, the setup was subjected to extensive tests of the performance of all key elements most important of which are: tests on probe beam extinction ratio by AOM, EOM modulation performance, beat note between the probe laser and OFC stability observations and linearity of the detection system including detector and the analog to digital converter (ADC) board. The nonlinearity of the detection system was estimated based on a comparison between measurements with CRDS and CMWS techniques of oxygen lines reported in Ref. [63]. It was found with simulations that the most common types of nonlinearities affect the line intensity determined with those two techniques in the opposite way. The simulated decay of the ring-down or cavity mode shape was modified by multiplying it with either function $w_1(U) = 1 - a \cdot U/U_{\max}$ or $w_2(U) = (U/U_{\max})^a$. In both functions, U represents the measured signal, $U_{\max}$ denotes its amplitude, and the a parameter quantifies the level of nonlinearity of the light intensity detection system. By comparing the results of obtained line intensities of oxygen lines with CRDS and CMWS techniques the maximal value of possible nonlinearity of the detection system was estimated to be 0.0035 and the maximal relative error on the line intensity due to this nonlinearity has the same value.

The raw signal from the detector needs to be trimmed by t_{start} at the start and by t_{end} at the end of acquisition before approximating it with the exponential function 1.4. It is done to minimize the effect of any transitional processes, for example from finite probe beam switch-off time, before t_{start} and to discard part after t_{end}, where there is effectively no signal. Figure 2.4 shows the RD signal measured with the probe detector (DET_P) after switching off the probe beam pumping of the RDC. The sharp structures in the fit residuals, visible on the figure 2.4 at 250 μs and below, are caused

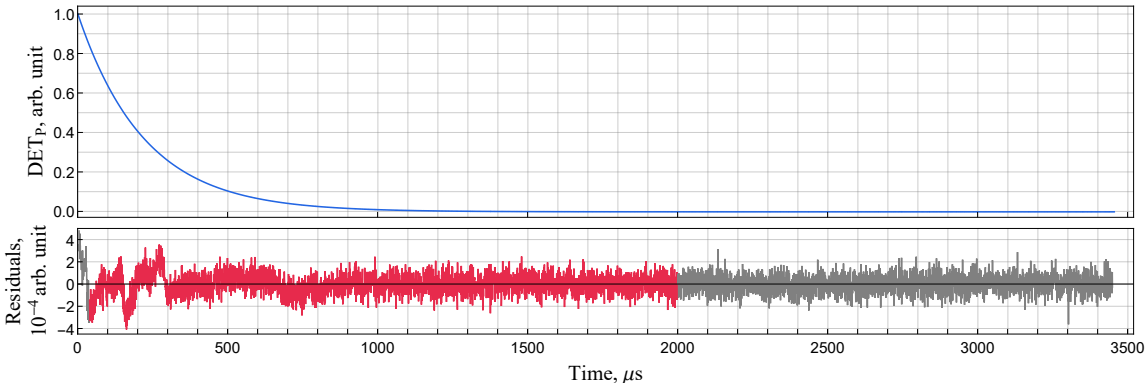

Figure 2.4: Top panel: Signal from the probe beam detector (DET_P) plotted against time shows the process of decaying intensity of the light leaking from the RDC. Bottom panel: Residuals of approximation of signal above by exponential function (equation (1.4)). The red color indicates the region that was chosen for τ_{RD} determination in CO measurements, while data marked in grey color were omitted during approximation.

by the automatic switching of measurement range done by the measurement board. The values of t_{start} and t_{end} were chosen empirically to minimize the sensitivity of the determined value of τ_{RD} to the changes of t_{start} and t_{end}. Figure 2.5 shows how the τ_{RD} depends on these parameters. Using values of t_{start} below 30 μs or t_{end} below 1500 μs

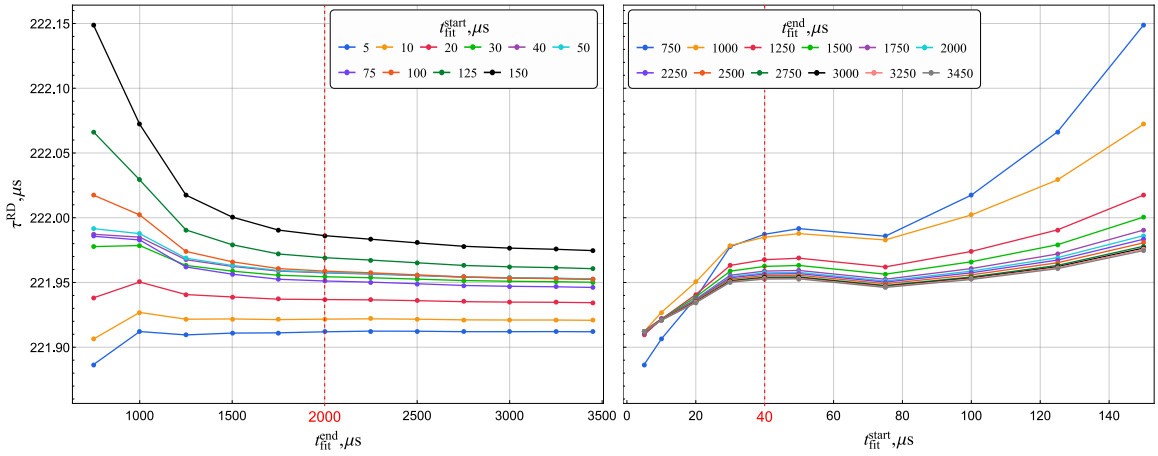

Figure 2.5: Dependency of determined τ_{RD} on the t_{start} – on the right plot and on t_{end} – on the left. Vertical red dashed lines show values that were used for the measurements of CO lines.

causes big variability of the determined τ_{RD}. For the measurement of 6th overtone

lines of CO values for the t_{start} and t_{end} were chosen 40 μs and 2000 μs respectively, as indicated by red dashed lines in fugure 2.5. For the $t_{\text{start}} = 40\mu$s, values of τ_{RD}, determined with all t_{end} except the two smallest values of 750 and 1000 μs had the same values with a maximal relative difference of less than 0.01 ‰. For chosen t_{end} of 2000 μs, the maximal relative difference of the τ_{RD} is more than 0.3 ‰ for the t_{start} from 5 to 150 μs and is reduced to less than 0.03 ‰ for the t_{start} from 30 to 75 μs.

From this set of tests, I concluded that for relatively large τ_{RD} (as in the case of this work) to correctly determine τ_{RD} one should omit part of the decaying signal much less than τ_{RD} (in the case of this work from 4 to 5.5 times) and record signal for much longer than τ_{RD} (in case of this work approximately 10 times).

The modified Allan variance analysis was done to determine an optimal number of RD time constant τ_{RD} measurements at each frequency. Figure 2.6 shows the dependency of Allan variance of τ_{RD} on the number of measurements with three different sampling rates of individual RD decay records. The sampling rate indicated on the figure's legend, is measured in Megasamples (1 million samples) per second (MS/s). Even though at 1000 records of RD decay the deviation of determined τ_{RD} is not reaching the minimum, this number of records was chosen for the measurements settings to not extend spectra acquisition time.

The performance of the system was confirmed by significantly increased, compared to previous studies, spectra SNR that allowed simultaneous observation of speed dependence and Dicke narrowing in the study of self-perturbed lines of oxygen B-band [63], that was done before carbon monoxide measurements.

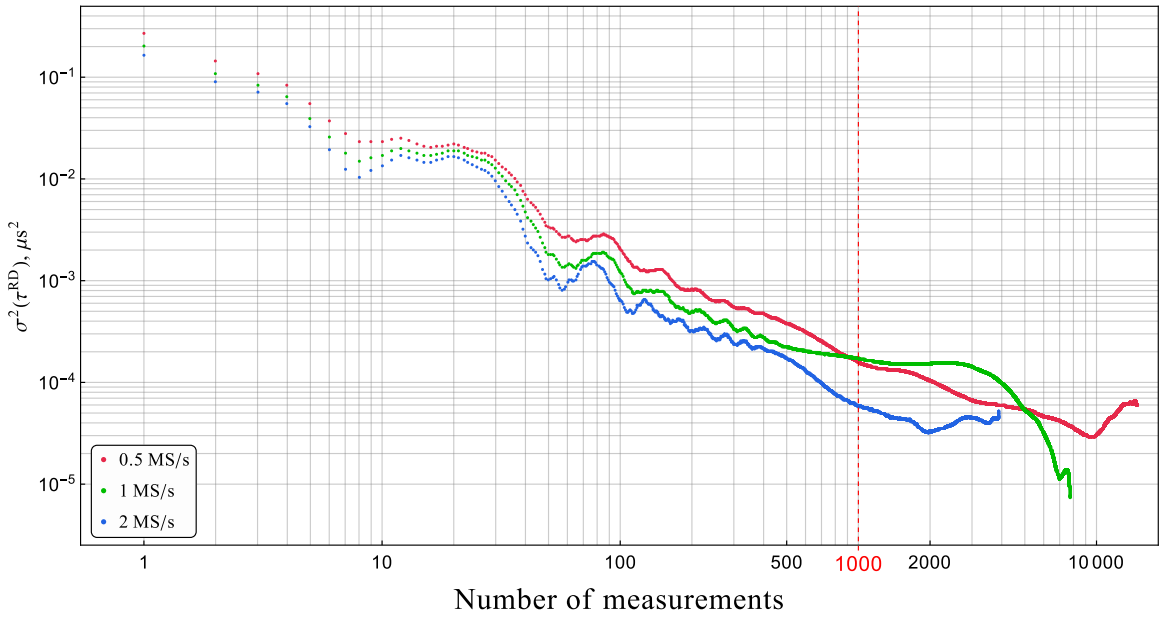

Figure 2.6: The modified Allan variance plots for different sampling rates of measurement. An average of three measurements for each sampling rate is shown. Red dots show the result for the sampling rate of 0.5 MS/s of individual RD decay measurement, green − for 1 MS/s and blue − for 2 MS/s. The vertical dashed red line indicates the number of RD signals averaged at each frequency.

CHAPTER 3

Analysis of experimental data

3.1. Line profile

The simplest way to quantitatively represent the spectrum of the gas is by its spectrum diagram. A spectrum diagram is a list of delta functions at the frequencies of allowed transitions of the molecules. The amplitudes of those delta functions represent the integrated line intensities normalized to the number of molecules S or line intensity for short, and as well as transition frequencies they are determined only by the properties of individual molecules. In atmospheric applications, broadband spectra are represented as a sum of resonant lines on top of the continuum absorption − excessive empirical absorption that cannot be explained by the sum of observed lines [64–67], having their shape determined by Doppler broadening and collisional perturbations. Continuum absorption includes bimolecular absorption, but the exact contribution of all its components remains unknown (Ref. [68] and references therein). Bimolecular absorption can be divided into three components: free pairs, metastable (quasi-bound), and stable (bound) dimers [69]. The contributions of these parts to bimolecular absorption can differ greatly for different molecular systems and thermodynamic parameters [70, 71]. Also included in the continuum is a part of the resonant absorption associated with the far wings of the lines. The behavior of the resonance line wings at distances from the center much greater than the characteristic line width is still unknown, and all current line profiles are valid only near their center [72, 73]. The resonant part of the absorption is modeled as a spectrum diagram to which the

shape of individual lines is applied:

$$\alpha(\nu) = \sum_k N \cdot S_k \cdot I(\nu, \nu_{0,k}), \tag{3.1}$$

where α is the absorption coefficien at frequency ν, N is the number of molecules, I is the function describing the shape of the line normalized to unity, $\nu_{0,k}$ is the central frequency of the k^{th} line and S_k is its intensity. The choice of the exact shape of the lines depends on the conditions of observation.

The simplest line profile commonly used in molecular spectroscopy is the convolution of the Lorentzian and Gaussian functions that is called Voight profile (VP), $\mathrm{I_{VP}}$. It combines two physical effects that cause the broadening of the line: collisional and Doppler broadening in their simplest approximations. Collisional broadening is related to the decrease of the lifetime of the molecular level resonant with the field due to state-changing collisions. According to the time–energy uncertainty relation $\Delta E \cdot \Delta t \geq \frac{\hbar}{2}$, where $\hbar$ is the reduced Planck constant, derived from Heisenberg's uncertainty principle, the finite lifetime of the level will lead to the non-zero uncertainty of the energy of the corresponding level. Additionally, phase-changing collisions, that do not change the state of the molecule, but perturb the phase of oscillation (emitted radiation), cause in general both a broadening and a shift of the radiation spectrum. The corresponding shape of the line profile is described by the Lorentzian function [74]. Doppler broadening is related to the fact that in the thermodynamic equilibrium, molecules move in all directions with velocities described by the Maxwell-Boltzmann distribution. The velocity distribution is given by:

$$f_{\mathrm{MB}} = \left(\frac{M}{2\pi k_{\mathrm{B}} T}\right)^{\frac{3}{2}} \exp\left(-\frac{M v^2}{2 k_{\mathrm{B}} T}\right), \tag{3.2}$$

where M is the molecular mass of the gas, T is the temperature in Kelvin, k_{B} is Boltzmann constant and υ is the speed of the molecule. This means that at non-zero detuning from the transition frequency of the electromagnetic field in the gas, there will be molecules that have a projection of the velocity on the direction of radiation propagation such that the corresponding Doppler shift will cancel detuning, and they will sense radiation at transition frequency. Line width related to the Doppler effect can be calculated using following equation:

$$\Gamma_{\mathrm{D}} = 2\sqrt{2 \cdot \ln(2)} \cdot \frac{\nu_0}{c} \sqrt{\frac{k_{\mathrm{B}} T}{M}}, \tag{3.3}$$

where Γ_{D} is the Doppler line width FWHM in hertz, ν_0 is the transition frequency in hertz. Profile corresponding to the Doppler broadening with accuracy to normalization factor is described by Gaussian profile [74].

Voigt profile is the real part of the complex Voigt profile

$$I_{\mathrm{VP}}(\nu) = \mathrm{Re}(\mathcal{I}_{\mathrm{VP}}(\nu)), \tag{3.4}$$

that can be written as follows:

$$\mathcal{I}_{\mathrm{VP}}(\nu) = \frac{1}{\pi} \int \frac{f_{\mathrm{MB}}(\vec{v})}{\Gamma - i[\nu - \nu_0 - \Delta - \frac{\vec{k}}{2\pi} \cdot \vec{v}]} \, d\vec{v}, \tag{3.5}$$

where Γ is collisional width, ν_0 is unperturbed transition frequency, Δ is collisional shift, $\vec{k}$ is the wave vector of the emitted radiation ($k = 2\pi\nu_0/c$, c is the speed of light). As it has been said VP can be represented by the convolution of Lorentzian and Gaussian profiles (see Appendix A.2) thus, these two mechanisms - collisional broadening and Doppler one are considered acting independently, which is an ap-

proximation having significant limitations.

It is worth noting that even for a single stationary molecule when there are no collisions and Doppler effect, the shape of the line will not be a delta function. The line will have its natural line width related to the finite lifetime of the levels due to spontaneous emission. As with collisional broadening the corresponding line shape will be Lorentzian function with FWHM Γ_{N} proportional to the Einstein coefficient for the spontaneous emission A_{ab}. For the case of this work the natural width of the line will be neglected because according to the data on A_{ab} in high-resolution transmission molecular absorption database (HITRAN) [45] for the transitions of the $(7-0)$ band of CO natural line width is on the level of 10^{-8} Hz, whereas in the measurement conditions, the Doppler width is about 1 GHz and the collisional broadening varies between 0.25 and 6 GHz.

It is obvious that the frequency of collisions depends on molecule speed. This means that collisional broadening and shifting coefficients will have speed dependence (SD), too. To determine the mean rate of collisions, one should average its distribution function over the distribution of speeds of molecules which we consider to be Maxwellian.

$$G_0 = \int G(\upsilon) f_{\mathrm{MB}}(\upsilon) d\upsilon, \tag{3.6}$$

where G is either collisional broadening Γ or shift Δ. The functional form of broadening and shift $-$ $G(\upsilon)$ (assuming that the long-range wing of the interaction potential is a power function) can be approximated [75] by quadratic functions as:

$$\begin{aligned} \Gamma(\upsilon) &= \Gamma_0 + \Gamma_2 \left(z^2 - \frac{3}{2} \right), \\ \Delta(\upsilon) &= \Delta_0 + \Delta_2 \left(z^2 - \frac{3}{2} \right), \end{aligned} \tag{3.7}$$

where Γ_2 and Δ_2 are empirical parameters describing the SD of the thermally averaged over the Maxwellian distribution collisional width Γ_0 and collisional shift Δ_0, respectively and z is reduced absorber velocity:

$$z = \left(\frac{\upsilon}{\upsilon_{\mathrm{m}}}\right) \tag{3.8}$$

where $\upsilon_{\mathrm{m}} = \sqrt{2k_{\mathrm{B}}T/M}$ is the most probable velocity of the molecule with the mass m. Alternatively, equations (3.7) can be rewritten as:

$$\begin{aligned} \Gamma(\upsilon) &= \Gamma_0 \cdot B_{\mathrm{W}}(z), \quad B_{\mathrm{W}}(z) = 1 + a_{\mathrm{W}}\left(z^2 - \frac{3}{2}\right), \\ \Delta(\upsilon) &= \Delta_0 \cdot B_{\mathrm{S}}(z), \quad B_{\mathrm{S}}(z) = 1 + a_{\mathrm{S}}\left(z^2 - \frac{3}{2}\right), \end{aligned} \tag{3.9}$$

where $a_{\mathrm{W}} = \Gamma_2/\Gamma_0$ and $a_{\mathrm{S}} = \Delta_2/\Delta_0$ are dimensionless parameters describing speed dependence of Γ_0 and Δ_0 respectively. The complex speed-dependent Voigt profile with quadratic approximation of speed dependence (qSDVP) [76] is expressed by:

$$\mathcal{I}_{\mathrm{qSDVP}}(\nu) = \frac{1}{\pi}\int \frac{f_{\mathrm{MB}}(\vec{v})}{\Gamma(\upsilon) - i[\nu - \nu_0 - \Delta(\upsilon) - \frac{\vec{k}}{2\pi}\cdot\vec{v}]}\, d\vec{v}, \tag{3.10}$$

So far, I have considered collisions that change the state of the molecule. However, during some of the collisions, a molecule can change only its velocity, staying on the same molecular level. The change of molecule's velocity direction during these collisions will statistically reduce velocity projection on the direction of radiation propagation. A decrease in the velocity will decrease the Doppler effect, effectively narrowing the line. This effect is called the effect of Dickie narrowing (DN) by the name of its discoverer [77]. The parameter describing this effect is the frequency of optical collisions, ν_{opt}. Its upper limit can be estimated from the mass diffusion

coefficient [78–81] as such:

$$\nu_{\text{dif}} = \frac{k_B T}{MD}, \tag{3.11}$$

where D − mass diffusion coefficient. For CO molecule $D = 0.192$ cm^2/s is calculated using first-order approximation [82]. When modeling line shapes with DN, different models of velocity-changing collisions can be used. The soft collision model assumes that individual velocity-changing collisions are negligible but collectively are significant, and the emitter motion can be described in terms of the theory of Brownian motion as a stochastic process. This model was first studied by Galatry in 1961 [83] thus corresponding profile was named Galatry profile (GP). Another approach is the hard collision model, when the velocity of the molecule after the collision is dependent only on the last collision. In other words, the molecule forgets its velocity after each collision. This approach was first described by Nelkin and Ghatak [84] in 1964, yielding a Nelkin-Ghatak profile (NGP) that is sometimes referred to as Rautian profile [78]. The speed-dependent Nelkin-Ghatak profile with quadratic approximation of speed dependence (qSDNGP) can be written as follows:

$$\mathcal{I}_{\text{qSDNGP}}(\nu) = \frac{\mathcal{I}^*_{\text{qSDVP}}(\nu)}{1 - \pi \cdot \mathcal{V}_{\text{opt}} \cdot \mathcal{I}^*_{\text{qSDVP}}(\nu)}, \tag{3.12}$$

where $\mathcal{I}^*_{\text{qSDVP}}(\nu)$ is profile $\mathcal{I}_{\text{qSDVP}}(\nu)$ from equation (3.10) in which the width $\Gamma(\upsilon)$ is replaced by the sum $\Gamma(\upsilon) + \mathcal{V}_{\text{opt}}$ (this change is designated by an asterisk).

I should mention that DN affects only the Doppler width of the line, thus this effect will have more significance at relatively low pressures when the collisional width is less or about the Doppler one. In these conditions, both SD of pressure broadening and DN affect the line shape similarly - as a narrowing of the profile, and it is difficult to distinguish between them, even at high SNR.

Table 3.1: Parameters and limiting cases of HTP for the profiles used in this work.

Profile	Line shape parameters	Limits of HTP
qSDNGP	Γ_D, Γ_0,Δ_0, a_W, a_S, $\mathcal{V}_{opt}$	$\eta = 0$
qSDVP	Γ_D, Γ_0, Δ_0, a_W, a_S	$\eta = \mathcal{V}_{opt} = 0$
VP	Γ_D, Γ_0, Δ_0	$\eta = \mathcal{V}_{opt} = a_W = a_S = 0$

All aforementioned profiles are derived from the assumption that both, state or phase-changing and velocity-changing types of collisions are not correlated. However, if we consider that some collisions can change both the internal state of the molecule and its velocity, then these two processes can no longer be treated as uncorrelated. It will require us to include in the model the parameter η that would determine the level of correlation between phase and velocity-changing collisions. One of such models is Hartmann-Tran profile (HTP) [85]. This profile accounts for the speed dependence of pressure broadening and shift in quadratic approximation and Dickie narrowing effect. It uses the hard collision model for velocity-changing collisions and accounts for the correlation between phase and velocity-changing collisions. HTP was recommended by International Union of Pure and Applied Chemistry (IUPAC) as a profile going beyond the VP [86]. Even though it is a model line profile and thus it approximates the line shape, it was shown that HTP can model the line shape in a broad range of conditions with accuracy not worse than 0.1% of the peak absorption [87]. It is presently recommended that line parameters stored in the new-generation spectroscopic databases are compatible with the HTP. All profiles used in this work (VP, qSDVP, qSDNGP) are the limiting cases of HTP and can be derived from it by putting certain parameters to zero. Table 3.1 lists parameters and limiting cases of HTP for the profiles used in this work.

All aforementioned effects were described for isolated lines. Lastly, we consider another line shape effect that can affect only collisionally interacting (mixed) transitions.

If the molecule, due to collisions, can transit from the states of one transition to the states of the other, these two transitions can no longer be treated as independent. Molecules that undergo one transition will affect the population of levels of the second transition, directly affecting the intensity of the corresponding line. This effect is called line mixing [88], and it shows up on the spectra as a dragging of intensities to the frequency of the center of mass of mixed transitions and as additional line profile asymmetry, and the latter effect is easier to observe on the single line spectra. Line mixing is commonly included in the line-shape profile with the first-order [89] (linear on pressure) line-mixing coefficient Y and can be added in the same way to any of the profiles described in this work:

$$\mathrm{I}^{\mathrm{LM}}(\nu) = \mathrm{Re}\left((1 - iY)\mathcal{I}(\nu)\right), \tag{3.13}$$

where $\mathcal{I}(\nu)$ – is the complex line profile. The speed dependence of the line-mixing can be described in the same way as in equation (3.7) for collisional broadening Γ and shift Δ.

Pressure dependence of line parameters used in this work is as follows: the unperturbed line position ν_0 is constant while A, Γ_0, Δ_0, Γ_2, Δ_2, $\mathcal{V}_{\mathrm{opt}}$ and Y are assumed to vary linearly with concentration, which assuming ideal gas approximation at constant temperature is proportional to the pressure:

$$\begin{aligned} A(P) &= S \cdot P \\ \Gamma_{0,2}(P) &= \gamma_{0,2} \cdot P, \\ \Delta_{0,2}(P) &= \delta_{0,2} \cdot P, \\ \mathcal{V}_{\mathrm{opt}}(P) &= \nu_{\mathrm{opt}} \cdot P, \\ Y(P) &= y \cdot P. \end{aligned} \tag{3.14}$$

Here A is the line area, γ and δ – are coefficients of self-broadening and self-shift, respectively, ν_{opt} – is pressure-independent coefficient of frequency of optical collisions $\mathcal{V}_{\text{opt}}$, y – is pressure-independent coefficient of the line mixing parameter Y and P is the pressure of the gas. It means that line mixing is treated in the first-order approximation [89]. The Γ_{D}, a_{W} and a_{S} parameters are pressure independent.

The temperature dependence of line intensity is described [90] by:

$$S(T) = S(T_{\text{ref}})\frac{Q(T_{\text{ref}}) \cdot \exp(-hcE''/k_{\text{B}}T)}{Q(T) \cdot \exp(-hcE''/k_{\text{B}}T_{\text{ref}})} \cdot \frac{1 - \exp(-h\nu_0/k_{\text{B}}T)}{1 - \exp(-h\nu_0/k_{\text{B}}T_{\text{ref}})} \tag{3.15}$$

where E'' is the transition lower state energy and $Q(T)$ the total partition sum, both of which are available in the HITRAN database [45], and T_{ref} is the reference temperature. The consensus of the temperature dependence of other line parameters is not yet reached except for the pressure broadening Γ_0, for which the power law (equation (3.16)) has been adopted [85]. For the parameters Γ_2, Δ_0 and Δ_2 we assume the same function of temperature dependence:

$$\begin{aligned} \Gamma_{0,2}(T) &= \Gamma_{0,2}(T_{\text{ref}}) \cdot \left(\frac{T_{\text{ref}}}{T}\right)^{\eta_\gamma}, \\ \Delta_{0,2}(T) &= \Delta_{0,2}(T_{\text{ref}}) \cdot \left(\frac{T_{\text{ref}}}{T}\right)^{\eta_\delta}. \end{aligned} \tag{3.16}$$

where η_γ and η_δ are temperature-dependence parameters for $\Gamma_{0,2}$ and $\Delta_{0,2}$ respectively. Central line frequency ν_c at given pressure is described by:

$$\nu_c = \nu_0 + \Delta, \tag{3.17}$$

where ν_0 is unperturbed transition frequency (extrapolated to zero pressure).

3.2. Methods of experimental data analysis

Values of spectroscopic parameters retrieved from the experiment are obtained by multi-dimensional optimization made with the Levenberg-Marquardt algorithm [91]. The choice of line profile depends on the conditions of the experiment and the SNR of the data. Considering the relatively large amount of floating parameters and their cross-correlation for most advanced line profiles, requirements for the data to be successfully used with such profiles include not only a high level of the SNR but also a large range of pressures, ideally, such that the ratio of the collisional and Doppler width would span from $\Gamma_0/\Gamma_D \ll 1$ to $\Gamma_0/\Gamma_D \gg 1$.

Another important aspect of data analysis when using profiles with a high correlation of parameters is using a "multispectrum" fitting procedure [92–94] when all individual spectra are fitted simultaneously with the considered pressure dependence of parameters. Contrary to the "pressure-by-pressure" fitting when for each pressure, all pressure-dependent parameters are fitted individually and then approximated by corresponding pressure dependence (equation (3.14)).

Additionally, I will distinguish two approaches for multispectrum fitting. In the first that I will refer to as the individual line area approach, the line areas A (equation (3.14)) are fitted as individual parameters for each pressure. In the second approach, line area pressure dependency is assumed to be a linear function with zero-crossing at zero pressure. The second approach is considered to be more reliable because the expected dependency included in the model reduces the freedom of the fit and the correlation between the adjustable parameters, while the first one has the benefit of analysis of potential deviations of line area from a linear dependency. These deviations in general can be a test of the validity of the used line shape model or they could

be manifestations of the non-impact effects [95, 96]. In high-SNR conditions (above 1000) individual multispectrum fit is preferable, as it allows to account for potential nonlinearity of the pressure gauge [52, 63].

For quantification of the quality of the spectra approximation, the quality-of-the-fit factor (QF) is used [97, 98]. It is the ratio of maximal absorption of the gas in the measured spectra to the standard deviation of fit residuals and for single spectra fitting it is given by the following expression:

$$\mathrm{QF} = \frac{\mathrm{Max}_i \alpha_{\mathrm{line}}(\nu_i)}{SDF}, \tag{3.18}$$

where $\alpha_{\mathrm{line}}(\nu_{i,j})$ is the absorption coefficient, simulated with fitted line profile without the baseline at the i-th frequency point of the spectra, and SDF is the standard deviation of fit residuals, calculated in the following way:

$$SDF = \sqrt{\frac{\sum_i^W \alpha_{\mathrm{exp}}(\nu_i) - \alpha_{\mathrm{fit}}(\nu_i)}{W - r}}, \tag{3.19}$$

where α_{exp} and α_{fit} are values of the absorption coefficients measured in the experiment and calculated with the fitted profile, W is the total number of experimental points, and r is the number of fitted parameters in the model. For multispectrum fit, the quality-of-the-fit factor equal to the ratio of maximal absorption to the standard deviation of fit residuals across all pressures and is given by the following expression:

$$\mathrm{QF}_{\mathrm{multi}} = \frac{\mathrm{Max}_j \mathrm{Max}_i \alpha_{\mathrm{line}}(\nu_{i,j})}{SDF_{\mathrm{multi}}}, \tag{3.20}$$

where index j represents spectra measured at different pressures and SDF_{multi} is the

standard deviation of the combined spectra fit, calculated in the following way:

$$SDF_{\text{multi}} = \sqrt{\frac{\sum_j^M \sum_i^{W_j} \alpha_{\text{exp}}(\nu_{i,j}) - \alpha_{\text{fit}}(\nu_{i,j})}{\sum_j^M (W_j) - r_{\text{multi}}}}, \tag{3.21}$$

where M is the number of pressures and r_{multi} is the number of fitted parameters in the multispectrum model.

3.3. Apparatus function

As discussed in chapter 1, raw experimental spectra consist of two parts: one representing losses in the cavity due to absorption in gas and the other representing self-losses (baseline). In theory, the self-losses can be measured with the cavity filled with non-absorbing gas. It would require repeating the conditions of the first measurement precisely, which in practice is a very challenging task. The alternative solution is to account for the self-losses mathematically by including the model of the baseline in the fitting profile. This can be done if the absorption line is sufficiently well modeled and an appropriate model for the baseline is chosen.

The common approach for modeling baseline is to use a polynomial function to account for the broadband, compared to the line width, variations of the self-losses, which in the case of cavity-based spectroscopic techniques would be caused by the frequency dependence of mirrors reflectivity. Another components common for spectroscopy with optical resonator are etalon fringes [99]. Parasitic reflections of the light from external elements back to the ring-down cavity create unwanted interference, which appears on the spectra as a slow sinusoidal variation of the base losses [100]. Minimizing this effect to improve the detection limit of the setup is commonly done by utilizing wedged ring-down mirrors, tilted optics, and anti-reflective coatings on every optical interface. In the present work, also the Faraday isolator is placed in the

probe beam in front of the cavity, shown in figure 2.3, is used to reduce the etaloning effect. Nevertheless, in the setup used in this work etalons appear on the spectra and should be accounted for. The etalon effect is described by the Airy function, but for very low finesse it can be well modeled with the sine (or cosine) function as such:

$$Et(f) = C \cdot \sin\left(2\pi\frac{f}{\rho} + \phi\right), \tag{3.22}$$

where C, ρ, and ϕ are floating parameters representing amplitude, period, and the phase of the etalon.

CHAPTER 4

Measurements and results

This chapter presents the results of the first measurements of $(7-0)$ absorption band of CO. Measured lines are indicated in red in the figure 4.1 that shows the spectrum diagram of $(7-0)$ band according to the HITRAN2020 database [45]. The lines were

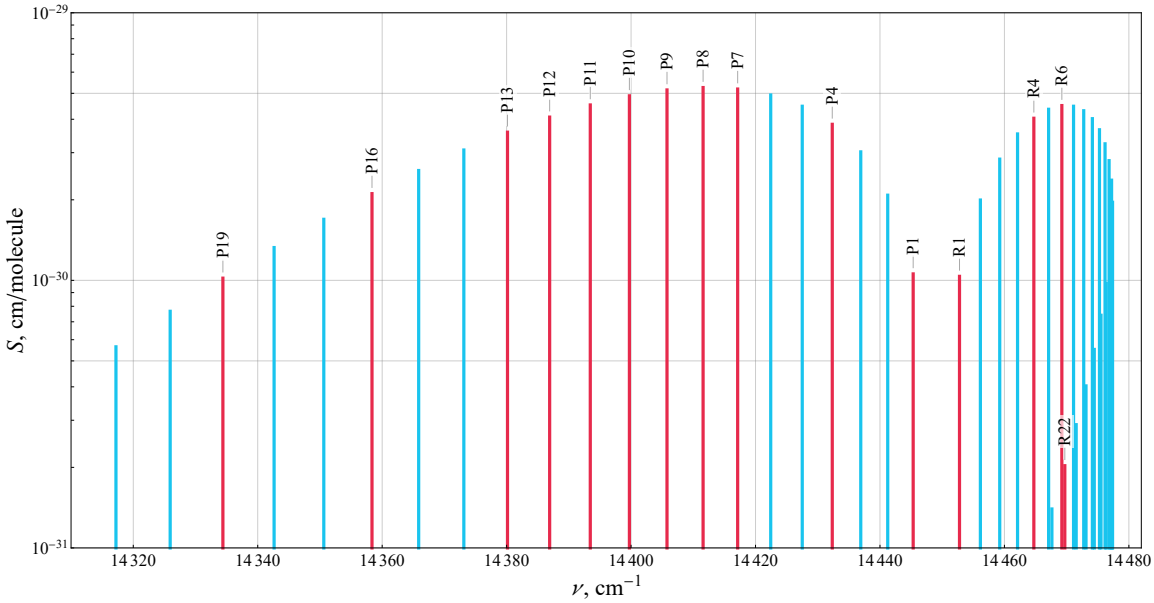

Figure 4.1: Stick-diagram of $(7-0)$ band of the main isotopologue of carbon monoxide according to the HITRAN2020. Corored in red are the lines that were measured in this work.

chosen to cover a broad range of J'' numbers. Some of the relatively strong lines were omitted due to proximity to the strong water or oxygen lines, as both these gases were present in the absorption cell in residual amounts. Most of the lines from the R branch were not measured because they would overlap at high pressures, which would complicate the analysis and decrease the accuracy of retrieved line parameters. In total 14 lines were studied using a high-purity carbon monoxide sample at natural isotopic abundance from Linde Gas with stated purity of 99.997%. The temperature

of the gas was actively stabilized at 296.000(35) K. Each line was measured at five pressures. Stronger lines (P13, P12, P11, P10, P9, P8, P7, P4, R4 and R6) were measured in the rage from 50 Torr (6.7 kPa) to Torr 750 (100 kPa), while weaker ones (P19, P16, P1, and R0) from 100 Torr (13.3 kPa) to 800 Torr (106.7 kPa). Each spectrum was about 30 GHz wide even for the measurements at the lowest pressures. This was done to record and properly analyze the spectra baseline, and especially to cover full period of each of etalons present in the baseline, see chapter 4.3 for more details. From 14 to 88 scans in forward and backward directions depending on the absorption (typically 20) were averaged for each pressure. The experimental spectra were analyzed using several well-known limits of the HTP [85] in particular the VP, qSDVP, and qSDNGP. For the analysis of experimental data, linear and individual approaches of multispectral analysis were used, described in chapter 3.2. Some spectra contain lines of water and oxygen, which are present in the system in residual amounts. Blended lines were assigned usind HITRAN2020 database to calculate the Doppler width. The H_2O and O_2 lines were approximated by the Voigt profile with the line area, line center, and line width fitted individually for each pressure since their content in the sample could change significantly due to adsorption/desorption processes from the internal surfaces of the vacuum system.

Due to very low line intensities, the absorption coefficient in the line peaks has relative magnitudes of only 0.07 % to 0.6 % of the spectrum baseline that represents losses that are not related to absorption in the gas. The range of measured absorption is shown in figure 4.2 that plots the average spectra of the weakest line measured in this work - P19 at the lowest pressure of 100 Torr and one of the strongest lines − P8 at the highest pressure of 750 Torr. Measured absorption, shown in the plots, corresponds to the change of RD time constant from 161.83 μs in the baseline to 160.99 μs in the

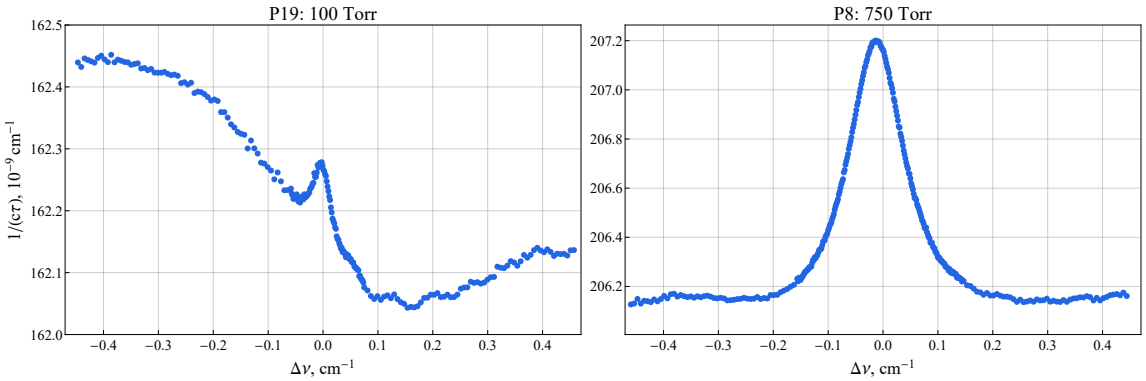

Figure 4.2: Left plot: average spectra of P19 line at 100 Torr. Right plot: average spectra of P8 line at 750 Torr. The horizontal axis is the frequency detuning ($\Delta\nu = \nu - \nu_0$) from the unperturbed line position.

peak absorption for P8 line at 750 Torr. The difference between absorption in the line center and line wing after removing baseline for P19 at 100 Torr corresponds to 0.15 μs difference in RD time constant while the amplitude of baseline itself is about 0.5 μs. The average value of τ_{RD} corresponding to the case of the empty cavity is approximately 220 μs. The large difference of values of τ_{RD} for different pressures is due to the geometrical changes of alignment of the probe beam caused by unbalanced mechanical stresses induced by the pressure difference of the gas inside and outside the absorption cell.

4.1. Line profile

The final analysis of experimental data was done by using qSDVP as it gave the best results in terms of reliability of determined line-shape parameters. To get to this conclusion a comparison of qSDVP with the results of VP and qSDNGP fits was made. The examination of spectra utilizing a simple Voigt profile, with an individual line area approach and neglecting speed-dependent effects (a_{W} and $a_{\mathrm{S}} = 0$), demonstrated a nonlinear dependence of line area on pressure for certain lines. Figure 4.3 displays this result. With the exception of line R6, this effect was observed primarily for lines with

relatively high intensity. The type A uncertainties for VP are significantly smaller than for qSDVP because there are fewer parameters and therefore less correlations between them. Regardless, employing VP would have caused the determined line intensity to depend on the pressure range of the measurement which is not expected at this level in this pressure range. Analyzing measurements with VP in the pressure range of the two lowest pressures would overestimate line intensities on average by 4.5 % while in the pressure range of the two highest pressures would underestimate line intensities on average by 0.5 %. The systematic nonlinear behavior of line area over pressure indicated that a more advanced line profile was required for this data, despite of relatively low SNR of the single pressure spectra, which was roughly 300 for the strongest transitions.

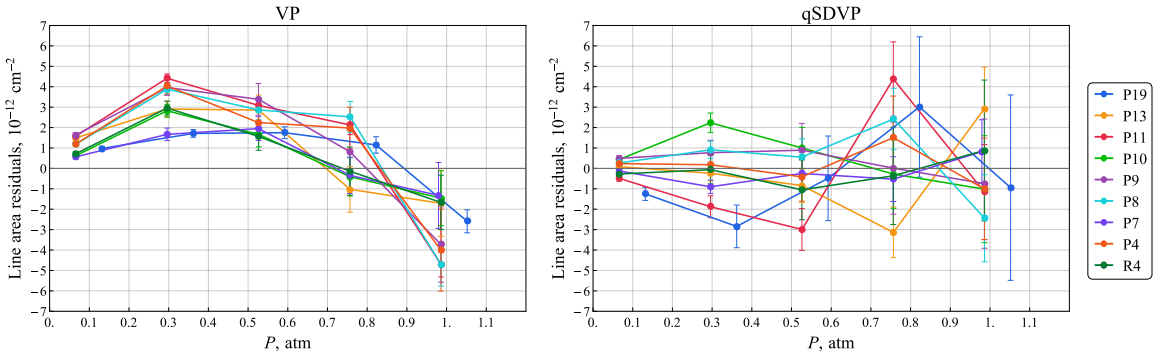

Figure 4.3: Residuals of line area linear approximation versus pressure for VP (left plot) and qSDVP (right plot) for lines indicated in the figure legend. The values of the line areas were obtained from the multispectrum fit using the individual line area approach described in chapter 3.2. Error intervals show type A standard uncertainty.

Comparing the qSDNGP fits with qSDVP revealed that the use of qSDVP is sufficient for this experimental data. The use of the more physically accurate qSDNG profile, which considers the frequency of velocity-changing collisions (i.e., Dickie narrowing effect), resulted in inferior results. This is due to the correlation between a_{W}, which is responsible for line narrowing due to speed dependence, and ν_{opt}, which is respon-

sible for line narrowing due to velocity-changing collisions. Figure 4.4 illustrates this correlation by plotting these parameters for considered lines. For qSDNGP results marked with blue dots (•) it is clearly visible that lines for which the values of ν_{opt} deviate from the average value, that is close to 0, have values of a_{W} deviate from its average, which is approximately 0.1, in opposite direction. Fitting with qSDVP (■) (effectively fixing ν_{opt} to 0) gives more consistent results for a_{W} across different lines. Though it is possible to have m-dependence for a_{W} values, dependencies obtained with qSDNGP analysis are not typical and it is unlikely that they are true.

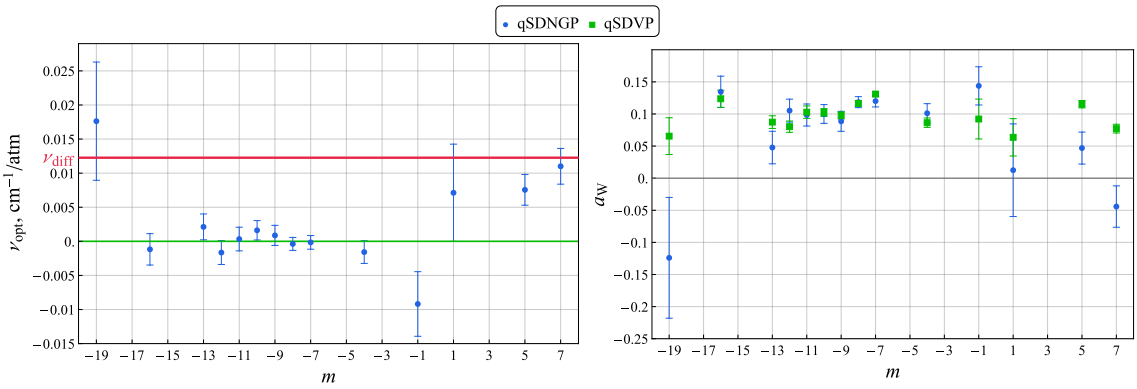

Figure 4.4: Plots of ν_{opt} (left) and a_{W} (right) values from fits using linear line area multispectrum approach with qSDNGP marked with blue dots (•) and qSDVP marked with green squares (■). Uncertainty intervals show only type A standard uncertainty. Red line shows the value of $\mathcal{V}_{\text{diff}}$ from equation (3.11), recalculated to the units of cm^{-1}/atm.

4.2. Baseline

At least two etalons on the baseline of the spectra were observed with periods of about 26 GHz and 17 GHz and amplitudes comparable to that of the line at low pressures. These etalons were formed by parasitic reflections from cavity mirrors and windows located inside a temperature-stabilized enclosure.

Furthermore, we noticed a quasi-periodic signal, that in this thesis will be referred to as the third etalon, with a period of 2.5 GHz that covered only part of the spectrum.

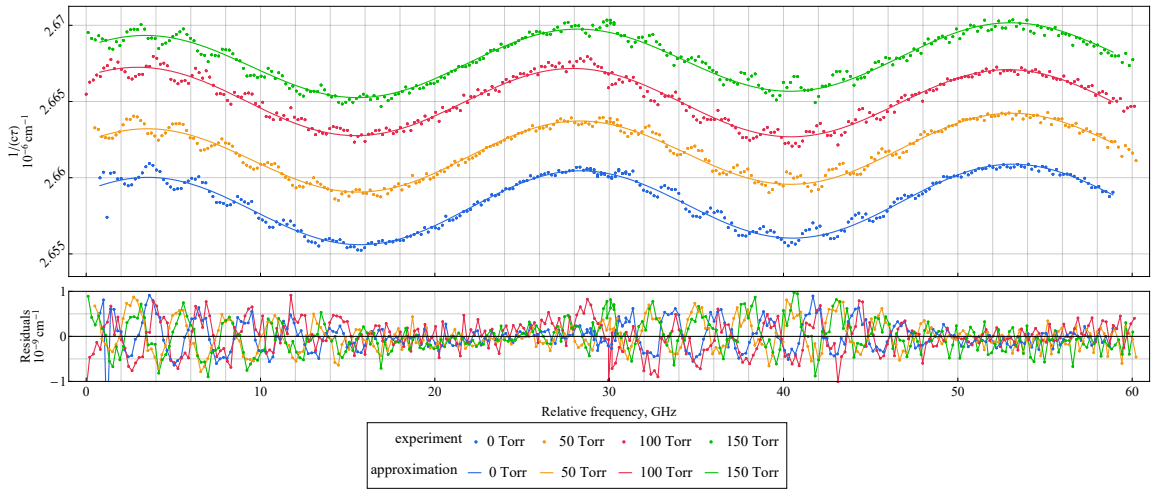

Figure 4.5: Dots on the top panel show the combined spectrum of cavity self-losses measured at four pressures with nitrogen. Solid lines show the approximation of the data without taking into account the third etalon. The bottom panel shows the residuals of the approximation.

The half-period of 1.3 GHz was close to the line width at low pressures, which raised concerns about the fit quality and systematic uncertainty of fitted line parameters. This quasi-etalon spectrum could be due to several interfering etalons with different periods. This assumption can be supported by measurements that were made after the measurements of CO lines in a close frequency range, with mirrors with lower reflectivity R of approximately 99.98%, in pure nitrogen. Figure 4.5 shows baseline measurements over a wider frequency range at three pressures of N_2 (50, 100, and 150 Torr) and a vacuum. The spectra at each pressure are composed of two separate records with a width of ∼35 GHz (limited by the characteristics of the laser), each of which is averaged over four individual scans. The amplitude modulation of the third etalon is clearly visible, confirming the assumption about its origin. The third etalon was formed by one of the cavity mirrors and elements outside the thermal enclosure, which led to changes in its parameters, mainly the phase, during measurements of CO, which lasted typically nine hours per pressure. This behavior can also be observed on the bottom panel of figure 4.5, where the residuals of the approximation of the

spectra without taking into account the third etalon are shown. In the CO data analysis, the third etalon was approximated with a function that consists of a sine function and envelope that was chosen empirically to better fit the experimental data. The envelope was made from a half-period-part of cosine function between zeros and equal to zero elsewhere. This function is characterized by its effective width and position. This form was chosen from considerations of possible beat note of two etalons with equal amplitudes and the difference between periods of 2.6 GHz. This would explain the amplitude modulation of 2.6 GHz etalon, but it would create similar increasing and decreasing oscillations after the envelope reaches 0, which most of the time was not observed on the spectra. This effect can be explained as an artifact of averaging many scans over one pressure measurement that lasted up to 40 hours (typically 9 hours) during which the frequency and especially the phase of the third etalon changed noticeably.

Averaged spectra at different pressures with corresponding etalons in the baseline and fit residuals on the example of the P10 line are shown in figure 4.6.

4.3. Uncertainty

Systematic deviations should not be normally distributed, so for lack of a better assumption, it is recommended [101] to assume a rectangular distribution, for which the standard deviation is equal to maximum deviation divided by $\sqrt{3}$. To assess systematic uncertainties in the line intensity, the maximal difference of parameters from individual and linear line area multispectrum fit approaches of qSDVP fit was divided by $\sqrt{3}$. The resulting systematic uncertainty ranged from 0.11% to 16%, depending on the transition. On average, this was the largest contributor to the total line intensity standard uncertainty.

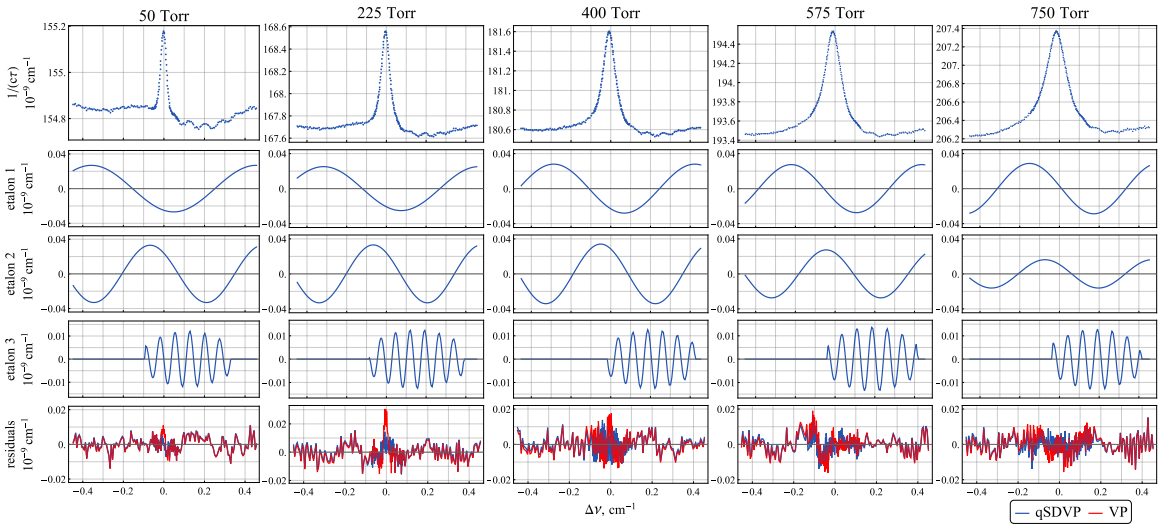

Figure 4.6: P10 line of CO measured at five different pressures, and temperature of 296 K. Top row shows raw averaged spectra with nominal pressures indicated above. Fitted etalons are shown in rows No 2, 3, and 4. The bottom row shows fit residuals for qSDVP in blue and for VP in red. The horizontal axis is the frequency detuning ($\Delta\nu = \nu - \nu_0$) from the unperturbed line position. Details in chapter 4.3.

To evaluate the impact of the baseline on the uncertainty of the fitted line parameters, a set of simulations was performed for over one hundred different configurations of observed etalons and line profiles. For the simulations, different values of line parameters in the expected range and different phases of etalons relative to the line center were used. Fitting simulated spectra was done in the same way as for the real experimental data. All simulations were done for two levels of SNR, corresponding to the case of the strongest and weakest transitions. It allowed to estimate how different line profiles, together with different configurations of the etalons, would affect retrieved parameter values for the experimental conditions and scale it for all the lines. The baseline-related uncertainty contributed from 2.2 % up to 13 % to the total standard uncertainty of line intensity and from 3.7 to 23 MHz of line position standard uncertainty, depending on the transition. The baseline on average was the largest contributor to the uncertainty of unperturbed line position and speed dependence of

pressure broadening.

To ensure that the total uncertainty was not underestimated, we added the uncertainty from the comparison of two measurements done for the P8 line. Repeated measurements were conducted in the same way for all pressures, more than one month after the first ones.

The uncertainty associated with the choice of line profile was estimated by comparing the results of qSDVP linear line area fit and VP fit also, with enforced linear dependence of line area on the pressure but with the baseline fixed to the values from qSDVP spectra analysis to not include effects of the baseline. The choice of line profile contributed from 0.6 % up to 1.8 % to the total standard uncertainty of line intensity and from 2 to 9 MHz of line position, depending on the transition. The uncertainty of other parameters cannot be estimated in this way, as collisional broadening and shifting obtained from these profiles have different physical meanings due to including or ignoring the SD effect.

Temperature and pressure measurement uncertainties contributed to the line intensity, pressure broadening, and shift uncertainties added less than 0.1 %. Temperature measurement uncertainty additionally affects its determination of the line intensity, pressure broadening, and pressure shift according to their expected temperature dependence (equations (3.15) and (3.16)). Corresponding contribution to the total uncertainty for these parameters is also below 0.1 %.

A detailed breakdown of the corresponding contribution to the uncertainty budget for qSDVP parameters is provided in the table 4.1 using the P10 line as an example. The estimated effect of the line mixing on the line intensity of CO was at the level of less than 0.26%. It was calculated by simulating spectra with qSDVP profile

Table 4.1: Detailed uncertainty budget of qSDVP parameters on the P10 line example. Contributions to the standard uncertainty of the unperturbed line position, ν_0, are given in 10^{-3} cm^{-1}, contributions to the standard uncertainties of all other parameters are given as relative values except for the a_{W} and a_{S}, for which it is absolute and dimensionless.

Uncertainty type	ν_0	S	γ_0	δ_0	a_{W}	a_{S}
Type A	0.067	0.003	0.0038	0.0095	0.0062	0.022
Contribution to B type uncertainty:						
frequency reference accuracy	0.000015	0.00008	0.00015	0.00071	—	—
temperature measurement	—	0.00012	0.00012	0.00012	—	—
temperature dependency	—	0.00032	0.00006	0.00006	—	—
pressure measurement	—	0.00013	0.00013	0.00013	—	—
choice of line profile	0.094	0.013	—	—	—	—
choice of multispectrum fitting procedure	0.033	0.016	0.016	0.012	0.021	0.00027
repeatability	0.029	0.018	0.019	0.037	0.0075	0.075
baseline model uncertainty	0.14	0.025	0.012	0.025	0.025	0.082
Total uncertainty	0.19	0.037	0.027	0.05	0.034	0.12

with line mixing (equation (3.13) with $\mathfrak{I}(\nu) = \mathfrak{I}_{\mathrm{qSDVP}}(\nu)$ from the equation (3.10)) and fitting it with qSDVP without line mixing. For simulations, the maximal value of the line mixing coefficient for transitions of $(7-0)$ band $Y = 0.02$ was taken from HITRAN2020. Pressure broadening coefficient γ_0 and its speed dependence parameter a_{S} were set to maximum observed values ($\gamma_0 = 0.094$ cm^{-1}/atm at reference temperature $T_{\mathrm{ref}} = 296$ K, $a_{\mathrm{S}} = 0.5$), as it should maximize the impact of line mixing. The error from the line mixing effect is safely below the stated total uncertainty.

For the pressure shift Δ_0 and its speed dependence parameter a_S, most of the uncertainty came from repeatability measurement and baseline simulations. For the pressure width Γ_0, the contribution of baseline simulations, repeatability, and systematic uncertainties from the comparison of multispectral fit approaches to the total uncertainty was similar. For the speed dependence parameter of pressure width a_W, baseline simulations and systematic uncertainties contributed the most of the total uncertainty. The uncertainty of the fit (type A) was always smaller than type B one for all transitions and parameters.

4.4. Results and discussion

The final values of parameters for all the lines were determined from qSDVP fitting with linear dependence of line intensity on the pressure and they are displayed in the table 4.2. As the Voigt profile is widely used in numerous applications, the set of parameters resulting from the VP analysis is presented in the table 4.3. To minimize the impact of the baseline on line shape for the VP fit, the values of baseline parameters were fixed to those obtained from qSDVP analysis. Note that fitting VP together with the baseline does not change the parameter's values significantly, i.e. more than their standard uncertainty.

The literature data on $(7-0)$ band of CO is quite scarce. The comparison of experimental results with data available in HITRAN2020 [45, 102] database is shown in figure 4.7. Plot a) of figure 4.7 shows absolute values of line intensity plotted against quantum number m, plot b) shows the differencies of unperturbed line positions from the corresponding values ν_0^{ref} from the HITRAN2020 database. Comparisons of absolute values for pressure broadening γ_0 and shift δ_0 and their SD parameters a_W and a_S with respective data from HITRAN are shown of panels c), d), e) and f) accordingly.

Table 4.2: Line-shape parameters obtained for all considered lines with qSDVP fit. Uncertainties given in parentheses are total standard uncertainties determined for each line and parameter. Unperturbed line position, ν_0, is given in cm^{-1}, line intensity S is in units 10^{-30} cm/molecule, collisional broadening γ_0 (half width at half-maximum (HWHM)) and shifting δ_0 coefficients are in cm^{-1}/atm at reference temperature $T_{ref} = 296$ K. Speed-dependent parameters a_W and a_S are dimensionless. QF is the quality-of-the-fit factor.

Line	ν_0	S	γ_0	δ_0	a_W	a_S	QF
P19	14334.40122(84)	1.81(38)	0.0616(107)	-0.0193(28)	0.065(44)	0.08(15)	36
P16	14358.36237(42)	3.65(27)	0.0624(26)	-0.0168(14)	0.124(36)	0.17(12)	76
P13	14380.14082(29)	6.70(27)	0.0653(19)	-0.0173(10)	0.087(35)	0.33(12)	124
P12	14386.91468(23)	7.53(31)	0.0656(19)	-0.0164(9)	0.080(35)	0.08(12)	136
P11	14393.44482(35)	9.07(37)	0.0683(22)	-0.0190(9)	0.103(35)	0.34(12)	138
P10	14399.73166(19)	9.59(35)	0.0677(18)	-0.0165(8)	0.102(34)	0.12(12)	190
P9	14405.77460(18)	10.65(36)	0.0698(17)	-0.0163(8)	0.098(34)	0.13(12)	184
P8	14411.57391(15)	10.99(37)	0.0714(17)	-0.0151(7)	0.117(34)	0.10(12)	249
P7	14417.12981(16)	11.03(37)	0.0728(17)	-0.0152(7)	0.131(34)	0.12(12)	248
P4	14432.33271(22)	8.45(32)	0.0778(20)	-0.0132(9)	0.086(34)	0.14(12)	157
P1	14445.33617(63)	2.54(27)	0.0939(57)	-0.0128(18)	0.092(46)	0.31(23)	37
R0	14452.78145(69)	2.46(28)	0.0899(65)	-0.0110(19)	0.064(44)	0.50(24)	42
R4	14464.72911(21)	9.12(32)	0.0746(17)	-0.0144(7)	0.115(34)	0.23(12)	183
R6	14469.22876(18)	9.99(35)	0.0688(17)	-0.0144(7)	0.077(34)	0.14(12)	169
R22	14469.70218(415)	0.91(37)	0.0877(131)	0.0126(100)	0.103[1]	0.17[1]	12

[1] a_W and a_S values for the R22 line were fixed to the mean values from the results of the other lines (see chapter 4.4 for details).

Table 4.3: Voigt profile line parameters for all considered lines (see details in chapter 4.3). Uncertainties given in parentheses are total standard uncertainties determined for each line. Unperturbed line position, ν_0, is given in cm^{-1}, line intensity S is in units $10^{-30}cm^{-1}/(molecule/cm^{-2})$, collisional broadening γ_0 (HWHM) and shifting δ_0 coefficients are in cm^{-1}/atm at reference temperature $T_{ref} = 296$ K. QF is quality-of-the-fit factor.

Line	ν_0	S	γ_0	δ_0	QF
P19	14334.40136(84)	1.78(38)	0.0597(107)	-0.0191(28)	41
P16	14358.36250(42)	3.59(27)	0.0599(26)	-0.0161(14)	77
P13	14380.14098(29)	6.64(27)	0.0639(19)	-0.0161(10)	124
P12	14386.91475(23)	7.45(31)	0.0640(19)	-0.0162(9)	144
P11	14393.44512(35)	8.97(37)	0.0666(22)	-0.0177(9)	130
P10	14399.73176(19)	9.47(35)	0.0656(18)	-0.0162(8)	178
P9	14405.77470(18)	10.52(36)	0.0678(17)	-0.0159(8)	178
P8	14411.57398(15)	10.82(37)	0.0688(17)	-0.0148(7)	204
P7	14417.12989(16)	10.83(37)	0.0696(17)	-0.0147(7)	194
P4	14432.33278(22)	8.36(32)	0.0760(20)	-0.0128(9)	160
P1	14445.33632(63)	2.51(27)	0.0916(57)	-0.0119(18)	43
R0	14452.78171(69)	2.45(28)	0.0889(65)	-0.0103(19)	48
R4	14464.72924(21)	8.99(32)	0.0721(17)	-0.0137(7)	164
R6	14469.22885(18)	9.88(35)	0.0672(17)	-0.0140(7)	173
R22	14469.70255(415)	0.85(37)	0.0833(131)	0.011(10)	12

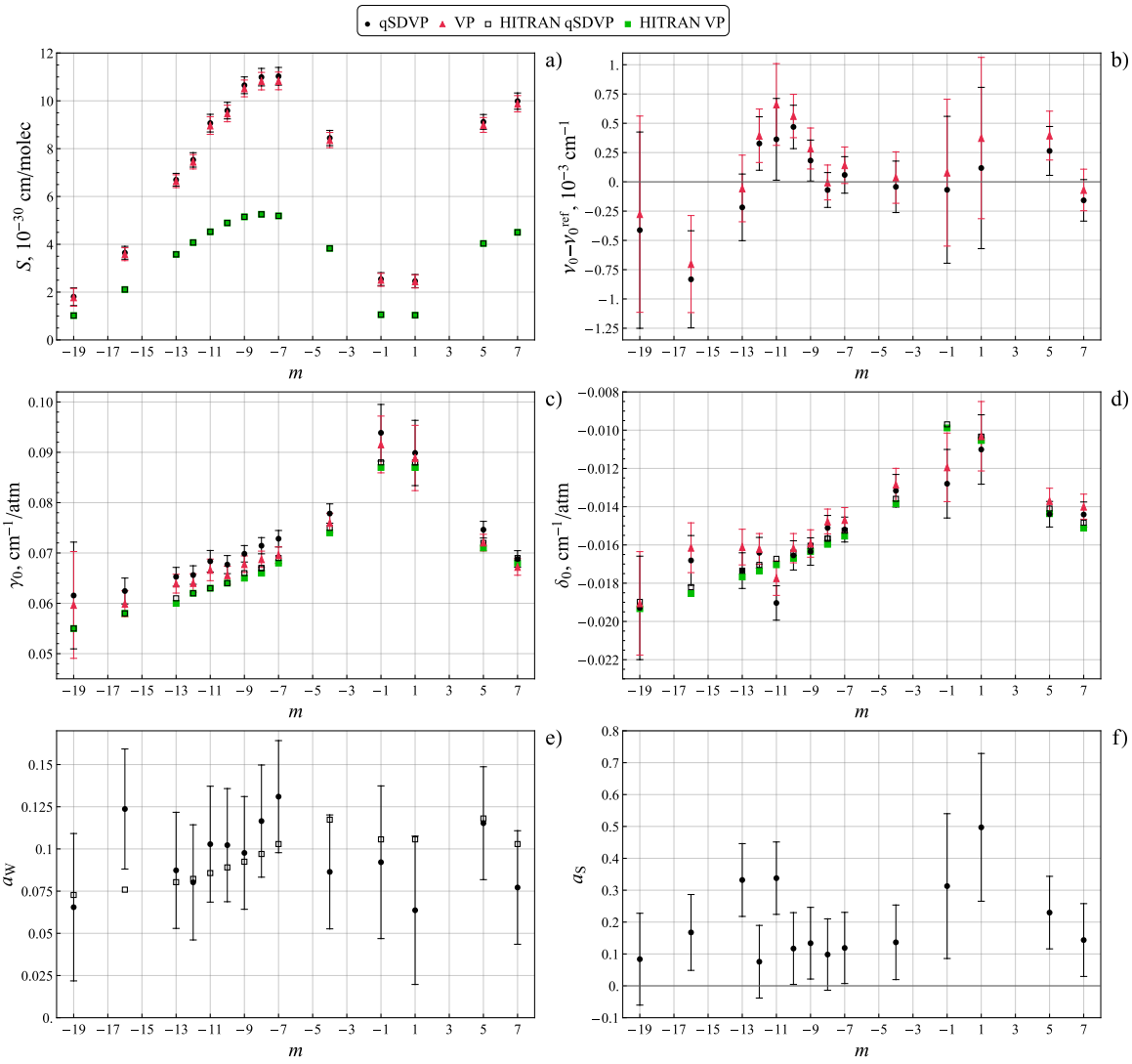

Figure 4.7: Comparison of experimental values using qSDVP (•) and VP (▲) of all determined line parameters with the reference data from HITRAN2020 database for qSDVP (□) and VP (■) against quantum number m. Panel a) shows absolute values of line intensity. Panel b) shows the difference between determined line positions and corresponding values of ν_0^{ref} from the HITRAN2020 database. Note that values for line position and intensity in HITRAN2020 are exactly the same for HITRAN VP and HITRAN qSDVP. Absolute values of pressure broadening and shift parameters are shown in panels c) and d), respectively. Error bars on the experimental data points correspond to the total standard uncertainty. Panel e) shows a comparison of the speed dependence of pressure broadening a_{W} for qSDVP fit with data available in the HITRAN2020. For the speed dependence of pressure shift a_{S}, only experimental data from this work is available and shown in panel f). Details in chapter 4.4

Line positions and intensities provided in HITRAN2020 are taken from a semi-empirical calculation by Li et al.[50], based on the PEC of Coxon and Hajigeorgiou[103] and DMC combined from a fit of best at that time experimental data of transitions from $(0-0)$ up to $(6-0)$ bands and spline-interpolation of their *ab initio* DMC for $(7-0)$ band and higher. The theoretical calculation underestimates intensities by about 100% (see panel a) of figure 4.7). Medvedev and Ushakov[43] showed that the use of splines for the PEC approximation leads to serious changes in the line intensities and showed that the purely empirical DMC of Li et al. [50] predicts intensity values in the $(7-0)$ band close to their most recent calculations [104]. The relative deviation:

$$\Delta S = \frac{S_{\text{Calculated}} - S_{\text{Measured}}}{S_{\text{Measured}}} \cdot 100\%. \tag{4.1}$$

from the experimental values of their results is shown in the figure 4.8 with the square dots.

High accuracy of measured intensities inspired new *ab initio* theoretical calculations carried out by the group of Dr. Oleg Polyansky at University College London (UCL). Measurements were part of a long-term project aimed at the development of a universal model capable of predicting intensities within experimental uncertainty for all the bands of a given molecule within a single set of calculations. Initial theoretical results using the same PEC that provided sub-promille-accurate line intensities of $(3-0)$ band [105] gave absurdly large discrepancy with the experiment of about 5000%. This triggered a detailed investigation of the problems of the model that allowed authors to identify bad points in the *ab initio* DMC caused by perturbative corrections. Removing bad points and interpolating the DMC to those points resulted in the *ab initio* DMC that reproduce experimental line intensities of $(7-0)$ band for almost all line intensities within one standard uncertainty of a few percent

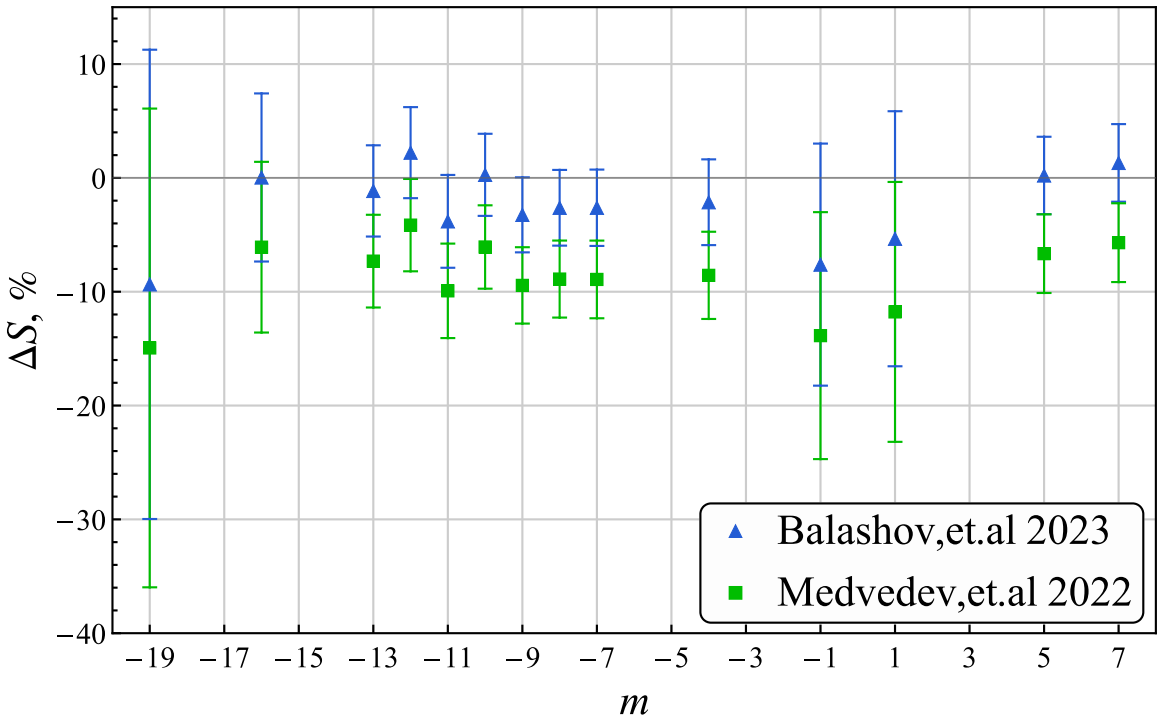

Figure 4.8: Difference between the experimental values of the line intensities of the 6^{th} overtone of CO obtained from the qSDVP analysis and the theoretical data from the work of Medvedev et al. [104] (■) and from [106] (▲). Difference calculated according to the equation 4.1

and lead to significant advancements in the development of a universal model for all the bands of CO. The detailed discussion of different theoretical calculations and difficulties accompanying the derivation of the final line intensities, the reader can find in paper [106]. The same PEC from Coxon and Hajigeorgiou [103] was used as in calculations currently available in HITRAN database, which reproduces the CO transition frequencies within standard uncertainty for most of the lines and within two standard uncertainties for all lines (see plot 4.7 b)).

It should be noted that the data for all line-shape parameters (except line position and intensity) in HITRAN2020 is an extrapolation of semi-empirical Padé approximant fits [102] of lower overtone measurements (up to the $(4-0)$). There are no direct measurements or calculations available for the considered transitions. This means

that comparison with this data will show only consistency across different overtones. Even though it was shown [102] that they do not depend on the overtone for lower bands this does not mean that it should be the same for higher overtones. Collisional broadening comparison with HITRAN qSDVP data shows (panel c) of the figure 4.7) good repeatability of the shape of its m-dependence, but data in HITRAN2020 underestimates the absolute values by about 5% on average. A slight increase in this difference with the decrease of m can also be observed. Panel d) of figure 4.7 shows pressure shift coefficient values that agree with HITRAN2020 data within the total standard uncertainty for most transitions.

The experimental results for a_{W} reported in panel e) of figure 4.7 for a_{W} agree with the overall trend observed for other overtones and agree within the total standard uncertainty with it. This additionally strengthens the selection of the qSDV profile for the final analysis. Since HITRAN2020 database does not provide the speed-dependent shift parameter values for any of the overtones, only present results are displayed in panel f) of figure 4.7.

Furthermore, the R22 line was observed as a blending transition together with the R6 line and was located at the edge of the scan. Figure 4.9 shows averaged spectra of R6 line measured in different pressures (top row) and fitted R22 line profile (second row). Due to large uncertainties resulting from fitting a_{W} and a_{S} under these conditions, their values were fixed to the average values obtained from other measured lines. The determined line parameters for the R22 line are presented in Tables 4.2 and 4.3, but have been omitted from the comparison of all line parameters with HITRAN2020 data shown in figure 4.7 for the sake of visual clarity as well as from the discussion of uncertainties and conclusions.

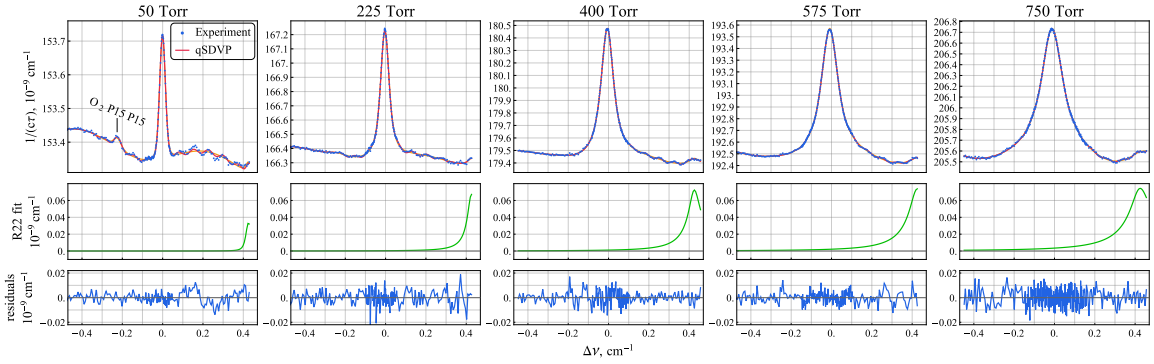

Figure 4.9: R6 line of CO measured at five different pressures, and temperature of 296 K. Oxygen P15 P15 B band line, visible on the spectra at 50 Torr of CO, was recorded as a blending transition and modeled with VP. The partial pressure of oxygen was estimated at the 0.4 ppm (parts per million) level. The top row shows averaged spectra with nominal pressures indicated above. Second row − R22 line fitted with qSDVP with fixed a_{W} and a_{S}. The bottom row shows fit residuals for qSDVP. The horizontal axis is the frequency detuning $\Delta\nu = \nu - \nu_0$ from the unperturbed line position of the R6 line. See details in the text (chapter 4.3).

CHAPTER 5

Conclusions

The most important results of the dissertation work are as follows.

1. For the measurement of the sixth overtone of CO, a CRDS spectrometer working in visible range (687 − 707 nm) was rebuilt to achieve sensitivity (noise-equivalent absorption) of $1.1 \cdot 10^{-9}$ cm^{-1}/s$^{1/2}$. The system of active temperature stabilization has been improved, which made it possible to control the temperature within 35 mK near 296 K. The analysis of the non-linearity of the detection system and the optimization of the recording parameters have been carried out.

2. First experimental study of rotational-vibrational transitions of the sixth overtone of carbon monoxide was conducted in the visible range near 690 nm. For 8 transitions, line intensity is determined with relative standard uncertainty below 4% and line positions with an accuracy of $3 \cdot 10^{-4}$ cm^{-1}. High accuracy of measured intensities inspired new *ab initio* calculations carried out by the group of Dr. Oleg Polyansky at UCL. Measurements were part of a long-term project aimed at the development of a universal model capable of predicting line intensities within experimental uncertainty for all the bands of a given molecule. The high quality of experimental data enabled significant advancement in this project and showed the excellence of resulted calculations compared to other works. They have also shown problems occurring in calculations and triggered their improvement. The measured line intensities, as well as the impact of measurements on calculations, are shown in Ref. [106].

3. A non-trivial approach to data processing made it possible to analyze the shape

of the lines beyond the Voigt profile approximation. Numerical simulations made it possible to increase the reliability of the uncertainty estimation of the determined line parameters. The parameters of self-broadening and pressure shift, are determined with a relative uncertainty of about 5% and are consistent with the values of the corresponding lines of lower-order overtones. Speed-dependence effects are observed and analyzed for the first time for such weak transitions.

During the course of my Ph.D. studies, more scientific results have been made that were not included in this thesis. Among them are: the Lamb-dip measurements of carbon dioxide line positions in saturation regime with CRDS, CMWS and Cavity Mode Dispersion Spectroscopy (CMDS) [107] techniques in IR range (paper is in preparation); search for extremely weak carbon dioxide transitions in the visible range (paper in preparation); measurements of self-perturbed oxygen B-band transitions that allowed simultaneous observations of Dickie narrowing and speed dependence effects [63]; as well as temperature measurements of oxygen B-band lines in air-like mixture with nitrogen [108].

All presented experimental data were obtained by the author personally or with his direct participation. The analysis of the experimental results of the study of the $(7-0)$ CO band and the development of the corresponding software was carried out by the author personally. The author actively participated in the construction of the present version of the CRDS spectrometer, which was used to acquire the CO $(7-0)$ band spectra. Theoretical calculations of line intensities of $(7-0)$ band of CO were provided by Nikolay F. Zobov in private communication. The author made a decisive contribution to the formulation of all the problems of the thesis, the formulation and conduct of experimental and numerical studies, as well as to the interpretation of the

results.

Appendices

Appendix A

Line profiles in dimensionless variables

For computational purposes, it is convenient to use dimensionless variables, when calculating line shape profiles.

A.1. Dimensionless variables

In this work for the data analysis I used line shape profiles described in chapter 3.1 and implemented in Wolfram Mathematica software. Profiles are implemented with dimensionless variables in accordance with the paper [109]. The dimensionless vari-

ables are defined as such:

$$\begin{aligned} u &= \frac{\nu - \nu_0}{\Gamma_{\mathrm{D}} / \left(2\sqrt{\ln 2}\right)}, \\ g &= \frac{\Gamma}{\Gamma_{\mathrm{D}} / \left(2\sqrt{\ln 2}\right)}, \\ d &= \frac{\Delta}{\Gamma_{\mathrm{D}} / \left(2\sqrt{\ln 2}\right)}, \\ h &= \frac{\mathcal{V}_{\mathrm{opt}}}{\Gamma_{\mathrm{D}} / \left(2\sqrt{\ln 2}\right)}. \end{aligned} \tag{A.1}$$

A.2. Voigt profile

Using equations (A.1) and (3.8) the equation (3.5) can be given in the form with dimensionless variables:

$$\mathfrak{I}_{\mathrm{VP}}(\nu) = \frac{1}{\pi^{3/2}} \int_{-\infty}^{+\infty} \frac{e^{-z^2}}{g - i\,(u - d - z)}\, dz. \tag{A.2}$$

Written in this form it is clearly visible that VP is the convolution of Lorentz and Gauss functions.

A.3. Speed-dependent Voigt profile

When collisional width and shift of the line are considered as dependent on the velocity of the molecule in the form, defined in the equations (3.9) one obtains qSDVP, that can be written in terms of dimensionless variables in the following way:

$$\begin{aligned} \mathfrak{I}_{\mathrm{qSDVP}}(u) = \frac{2}{\pi^{3/2}} \int_{-\infty}^{+\infty} z \cdot e^{-z^2} \cdot \\ \cdot \left\{ \arctan\left[\frac{u - d \cdot B_{\mathrm{S}}(z) + z}{g \cdot B_{\mathrm{W}}(z)}\right] + \frac{i}{2} \ln\left[1 - \left(\frac{u - d \cdot B_{\mathrm{S}}(z) + z}{g \cdot B_{\mathrm{W}}(z)}\right)^2\right] \right\} dz \end{aligned} \tag{A.3}$$

A.4. Speed-dependent Nelkin-Ghatak profile

Introduction of the DN effect to the qSDVP (equation (A.3)) results in qSDNGP, which in the form with dimensionless variables can be written as such:

$$\mathfrak{I}_{\mathrm{qSDNGP}}(u) = \frac{\mathfrak{I}^{*}_{\mathrm{qSDVP}}(u)}{1 - \pi \cdot h \cdot \mathfrak{I}^{*}_{\mathrm{qSDVP}}(u)}, \tag{A.4}$$

where $\mathfrak{I}^{*}_{\mathrm{qSDVP}}(u)$ is given by:

$$\begin{aligned}\mathfrak{I}^{*}_{\mathrm{qSDVP}}(u) = \frac{1}{\pi^{3/2}} \int_{-\infty}^{+\infty} z \cdot e^{-z^2} \cdot \\ \cdot \left\{ \arctan\left[\frac{u - d \cdot B_{\mathrm{S}}(z) + z}{g \cdot B_{\mathrm{W}}(z) + h} \right] + \frac{i}{2} \ln\left[1 - \left(\frac{u - d \cdot B_{\mathrm{S}}(z) + z}{g \cdot B_{\mathrm{W}}(z) + h} \right)^2 \right] \right\} \, dz\end{aligned} \tag{A.5}$$

List of publications

Publications comprising this thesis:

1. Balashov A.A., Bielska K., Li G., Kyuberis A.A., Wójtewicz S., Domysławska J., Ciuryło R., Zobov N.F., Lisak D., J.Tennyson, and Polyansky. O.L. Measurement and calculation of CO (7-0) overtone line intensities. *J. Chem. Phys.*, 2023. doi:10.1063/5.0152996. Accepted in volume 158.

Other publications:

1. Koshelev M.A., Leonov I.I., Serov E.A., Chernova A.I., Balashov A.A., Bubnov G.M., Andriyanov A.F., Shkaev A.P., Parshin V.V., Krupnov A.F., and Tretyakov M.Y. New frontiers in modern resonator spectroscopy. *IEEE Trans. Terahertz Sci. Technol.*, 8(6):773–783, 2018. doi:10.1109/TTHZ.2018.2875450.

2. Serov E.A., Balashov A.A., M. Yu. Tretyakov, Odintsova T.A., Koshelev M.A., Chistikov D.N., Finenko A.A., Lokshtanov S.E., Petrov S.V., and Vigasin A.A. Continuum absorption of millimeter waves in nitrogen. *J. Quant. Spectrosc. Radiat. Transfer*, 242:106774, 2020. doi:10.1016/j.jqsrt.2019.106774,

3. Bielska K., Domysławska J., Wójtewicz S., Balashov A., Slowiński M., Piwiński M., Cygan A., Ciuryło R., and Lisak D. Simultaneous observation of speed dependence and dicke narrowing for self-perturbed P-branch lines of O2 b band. *J. Quant. Spectrosc. Radiat. Transfer*, 276:107927, 2021. doi:10.1016/j.jqsrt.2021.107927.

4. Odintsova T.A., Serov E.A., Balashov A.A., Koshelev M.A., Koroleva A.O., Simonova A.A., M. Yu. Tretyakov, Filippov N.N., Chistikov D.N., Finenko A.A., Lokshtanov S.E., Petrov S.V., and Vigasin A.A. CO2–CO2 and CO2–Ar continua at millimeter wavelengths. *J. Quant. Spectrosc. Radiat. Transfer*,

258: 107400, 2021. doi:10.1016/j.jqsrt.2020.107400.

5. Serov E., Stolarczyk N., Makarov D., Vilkov I., Golubiatnikov G., Balashov A., Koshelev M., Wcisło P., Thibault F., and Tretyakov M. Co-ar collisions: ab initio model matches experimental spectra at a sub percent level over a wide pressure range. *J. Quant. Spectrosc. Radiat. Transfer*, 272:107807, 2021. doi:10.1016/j.jqsrt.2021.107807.

6. Bielska K., Tran D., Balashov A., Domyslawska J., Wójtewicz S., Bober M., Bilicki S., Ciuryło R., and Lisak D. Pressure and temperature dependencies of air-perturbed O2 B-band line shapes. *Spectrochim. Acta A*, 2023. in preparation.

Bibliography

[1] Greenberg O.W. Particles with small violations of fermi or bose statistics. *Phys. Rev. D*, 43:4111–4120, 1991. doi:10.1103/PhysRevD.43.4111.

[2] Mazzotti D., Cancio P., Giusfredi G., Inguscio M., and De Natale P. Search for Exchange-Antisymmetric States for Spin-0 Particles at the 10^{-11} level. *Phys. Rev. Lett.*, 86:1919–1922, 2001. doi:10.1103/PhysRevLett.86.1919.

[3] Santamaria L., Di Sarno V., Ricciardi I., Mosca S., De Rosa M., Santambrogio G., Maddaloni P., and De Natale P. Assessing the time constancy of the proton-to-electron mass ratio by precision ro-vibrational spectroscopy of a cold molecular beam. *J. Mol. Spectrosc.*, 300:116–123, 2014. doi:10.1016/j.jms.2014.03.013. Spectroscopic Tests of Fundamental Physics.

[4] Reinhold E., Buning R., Hollenstein U., Ivanchik A., Petitjean P., and Ubachs W. Indication of a cosmological variation of the proton-electron mass ratio based on laboratory measurement and reanalysis of h_2 spectra. *Phys. Rev. Lett.*, 96:151101, 2006. doi:10.1103/PhysRevLett.96.151101.

[5] Webb J.K., Murphy M.T., Flambaum V.V., Dzuba V.A., Barrow J.D., Churchill C.W., Prochaska J.X., and Wolfe A.M. Further evidence for cos-

mological evolution of the fine structure constant. *Phys. Rev. Lett.*, 87:091301, 2001. doi:10.1103/PhysRevLett.87.091301.

[6] Amato L.S., de Cumis M.S., Bianco G., Pastore R., and Pastor P.C. Linestrength ratio spectroscopy as a new primary thermometer for redefined kelvin dissemination. *New J. Phys.*, 21(11):113008, 2019. doi:10.1088/1367-2630/ab4d07.

[7] Wilson D.J., Gänsicke B.T., Farihi J., and Koester D. Carbon to oxygen ratios in extrasolar planetesimals. *Mon. Not. R. Astron. Soc.*, 459(3):3282–3286, 2016. doi:10.1093/mnras/stw844.

[8] Drummond J., Zou J., Nichitiu F., Kar J., Deschambaut R., and Hackett J. A review of 9-year performance and operation of the MOPITT instrument. *Advan. Sp. Res.*, 45(6):760–774, 2010. doi:10.1016/j.asr.2009.11.019.

[9] Eldering A., Wennberg P.O., Crisp D., Schimel D.S., Gunson M.R., Chatterjee A., Liu J., Schwandner F.M., Sun Y., O'Dell C.W., Frankenberg C., Taylor T., Fisher B., Osterman G.B., Wunch D., Hakkarainen J., Tamminen J., and Weir B. The Orbiting Carbon Observatory-2 early science investigations of regional carbon dioxide fluxes. *Science*, 358(6360):eaam5745, 2017. doi:10.1126/science.aam5745.

[10] Taylor T.E., Eldering A., Merrelli A., Kiel M., Somkuti P., Cheng C., Rosenberg R., Fisher B., Crisp D., Basilio R., Bennett M., Cervantes D., Chang A., Dang L., Frankenberg C., Haemmerle V.R., Keller G.R., Kurosu T., Laughner J.L., Lee R., Marchetti Y., Nelson R.R., O'Dell C.W., Osterman G., Pavlick R., Roehl C., Schneider R., Spiers G., To C., Wells C., Wennberg

P.O., Yelamanchili A., and Yu S. OCO-3 early mission operations and initial (vEarly) XCO_2 and SIF retrievals. *Remote Sens. Environ.*, 251:112032, 2020. doi:10.1016/j.rse.2020.112032.

[11] Kuze A., Suto H., Nakajima M., and Hamazaki T. Thermal and near infrared sensor for carbon observation Fourier-transform spectrometer on the Greenhouse Gases Observing Satellite for greenhouse gases monitoring. *Appl. Opt.*, 48(35):6716–6733, 2009. doi:10.1364/AO.48.006716.

[12] Suto H., Kataoka F., Kikuchi N., Knuteson R.O., Butz A., Haun M., Buijs H., Shiomi K., Imai H., and Kuze A. Thermal and near-infrared sensor for carbon observation Fourier transform spectrometer-2 (TANSO-FTS-2) on the Greenhouse gases Observing SATellite-2 (GOSAT-2) during its first year in orbit. *Atmos. Meas. Tech.*, 14(3):2013–2039, 2021. doi:10.5194/amt-14-2013-2021.

[13] Morse P.G., Bates J.C., Miller C.R., Chahine M.T., O'Callaghan F., Aumann H.H., and Karnik A.R. Development and test of the Atmospheric Infrared Sounder (AIRS) for the NASA Earth Observing System (EOS). In Fujisada H. and Lurie J.B., editors, *Sensors, Systems, and Next-Generation Satellites III*, volume 3870, pages 281 – 292. International Society for Optics and Photonics, SPIE, 1999. doi:10.1117/12.373196.

[14] Beer R. TES on the aura mission: scientific objectives, measurements, and analysis overview. *IEEE Trans. Geosci. Remote Sens.*, 44(5):1102–1105, 2006. doi:10.1109/TGRS.2005.863716.

[15] Clarisse L., Coheur P.F., Prata A.J., Hurtmans D., Razavi A., Phulpin T.,

Hadji-Lazaro J., and Clerbaux C. Tracking and quantifying volcanic SO_2 with IASI, the September 2007 eruption at Jebel at Tair. *Atmos. Chem. Phys.*, 8 (24):7723–7734, 2008. doi:10.5194/acp-8-7723-2008.

[16] Glumb R.J., Jordan D.C., and Predina J.P. Crosstrack infrared sounder (CrIS). In Strojnik M. and Andresen B.F., editors, *Infrared Spaceborne Remote Sensing VIII*, volume 4131, pages 108 – 119. International Society for Optics and Photonics, SPIE, 2000. doi:10.1117/12.406538.

[17] Sassen K. and Wang Z. Classifying clouds around the globe with the CloudSat radar: 1-year of results. *Geophys. Res. Lett.*, 35(4), 2008. doi:10.1029/2007GL032591.

[18] McGill M.J., Vaughan M.A., Trepte C.R., Hart W.D., Hlavka D.L., Winker D.M., and Kuehn R. Airborne validation of spatial properties measured by the CALIPSO lidar. *J. Geophys. Res.*, 112(D20), 2007. doi:10.1029/2007JD008768.

[19] Abendroth J.M., Bushuyev O.S., Weiss P.S., and Barrett C.J. Controlling Motion at the Nanoscale: Rise of the Molecular Machines. *ACS Nano*, 9(8): 7746–7768, 2015. doi:10.1021/acsnano.5b03367.

[20] Zeng G., Zhao J., Feng C., Chen D., Meng Y., Boateng B., Lu N., and He W. Flame-Retardant Bilayer Separator with Multifaceted van der Waals Interaction for Lithium-Ion Batteries. *ACS Appl. Mater. Interfaces*, 11(29):26402–26411, 2019. doi:10.1021/acsami.9b08553.

[21] Zhao G., Li X., Huang M., Zhen Z., Zhong Y., Chen Q., Zhao X., He Y., Hu R., Yang T., Zhang R., Li C., Kong J., Xu J.B., Ruoff R.S., and Zhu H. The

physics and chemistry of graphene-on-surfaces. *Chem. Soc. Rev.*, 46:4417–4449, 2017. doi:10.1039/C7CS00256D.

[22] Dame T., Hartmann D., and Thaddeus P. The Milky Way in molecular clouds: a new complete CO survey. *Astrophys. J.*, 547:792–813, 2001. doi:10.1086/318388.

[23] Visser R., Dishoeck E.F., and Black. J.H. The photodissociation and chemistry of CO isotopologues: applications to interstellar clouds and circumstellar disks. *Astron. Astrophys.*, 503:325–356, 2009. doi:10.1051/0004-6361/200912129.

[24] Connes P., Connes J., Kaplan L., and Benedict W. Carbon monoxide in venus atmosphere. *Astrophys. J.*, 152:731, 1968. doi:10.1086/149590.

[25] Bezard B., Debergh C., Crisp D., and Maillard J. The deep atmosphere of venus revealed by high-resolution nightside spectra. *Nature*, 345:508–511, 1990. doi:10.1038/345508a0.

[26] Owen T., Biemann K., Rushneck D., Biller J., Howarth D., and Lafleur A. The composition of the atmosphere at the surface of mars. *J. Geophys. Res.*, 82: 4635–4639, 1977. doi:10.1029/JS082i028p04635.

[27] Brogi M., de Kok R., Birkby J., Schwarz H., and Snellen I. Carbon monoxide and water vapor in the atmosphere of the non-transiting exoplanet HD 179949 b. *Astron. Astrophys.*, 565:A124, 2014. doi:10.1051/0004-6361/201423537.

[28] Konopacky Q., Barman T., Macintosh B., and Marois C. Detection of carbon monoxide and water absorption lines in an exoplanet atmosphere. *Science*, 339: 1398–1401, 2013. doi:10.1126/science.1232003.

[29] C. W. and P. S. Breath analysis using laser spectroscopic techniques: breath biomarkers, spectral fingerprints, and detection limits. *Sensors*, 9:8230–8262, 2009. doi:10.3390/s91008230.

[30] Beale C., Buzan E., Boone C., and Bernath P. Near-global distribution of CO isotopic fractionation in the Earth's atmosphere. *J. Mol. Spectrosc.*, 323:59–66, 2016. doi:10.1016/J.JMS.2015.12.005.

[31] Crutzen P., Heidt L., Krasnec J., Pollock W., and Seiler W. Biomass burning as a source of atmospheric gases CO, H_2, N_2O, NO, CH_3Cl and COS. *Nature*, 282:253–256, 1979. doi:10.1038/282253a0.

[32] Bernath P. The atmospheric chemistry experiment (ACE). *J. Quant. Spectrosc. Radiat. Transf.*, 186:3–16, 2017. doi:10.1016/j.jqsrt.2016.04.006.

[33] Veefkind J., Aben I., McMullan K., Förster H., de Vries J., Otter G., Claas J., Eskes H., de Haan J., Kleipool Q., van Weele M., Hasekamp O., Hoogeveen R., Landgraf J., Snel R., Tol P., Ingmann P., Voors R., Kruizinga B., Vink R., Visser H., and Levelt P. TROPOMI on the ESA sentinel-5 precursor: a GMES mission for global observations of the atmospheric composition for climate, air quality and ozone layer applications. *Rem. Sens. Environ.*, 120:70–83, 2012. doi:10.1016/j.rse.2011.09.027.

[34] Zelevinsky T., Kotochigova S., and Ye J. Precision test of mass-ratio variations with lattice-confined ultracold molecules. *Phys. Rev. Lett.*, 100(4):043201, 2008. doi:10.1103/PhysRevLett.100.043201.

[35] Hall D.N.B. Detection of the ^{13}C, ^{17}O, and ^{16}O isotope bands of CO in the infrared solar spectrum. *Astrophys. J.*, 182:977, 1973. doi:10.1086/152197.

[36] Förster Schreiber N.M. Moderate-resolution near-infrared spectroscopy of cool stars: a new k-band library. *Astron. J.*, 120(4):2089–2100, 2000. doi:10.1086/301568.

[37] Berthoud M.G., Keller L.D., Herter T.L., Richter M.J., and Whelan D.G. Near-IR CO overtone emission in 51 Ophiuchi. *Astrophys. J.*, 660(1):461–468, 2007. doi:10.1086/512056.

[38] Martins F., Pomarès M., Deharveng L., Zavagno A., and Bouret J.C. Near-IR integral field spectroscopy of ionizing stars and young stellar objects on the borders of H II regions. *Astron. Astrophys.*, 510:A32, 2010. doi:10.1051/0004-6361/200913158.

[39] GRAVITY collaboration: A. Caratti o Garatti, Fedriani R., Garcia Lopez R., Koutoulaki M., Perraut K., Linz H., Brandner W., Garcia P., Klarmann L., Henning T., Labadie L., Sanchez-Bermudez J., Lazareff B., van Dishoeck E.F., Caselli P., de Zeeuw P.T., Bik A., Benisty M., Dougados C., Ray T.P., Amorim A., Berger J.P., Clénet Y., Coudé du Foresto V., Duvert G., Eckart A., Eisenhauer F., Gao F., Gendron E., Genzel R., Gillessen S., Gordo P., Jocou L., Horrobin M., Kervella P., Lacour S., Le Bouquin J.B., Léna P., Grellmann R., Ott T., Paumard T., Perrin G., Rousset G., Scheithauer S., Shangguan J., Stadler J., Straub O., Straubmeier C., Sturm E., Thi W.F., Vincent F.H., and Widmann F. The GRAVITY young stellar object survey. II. First spatially resolved observations of the CO bandhead emission in a high-mass YSO. *Astron. Astrophys.*, 635:L12, 2020. doi:10.1051/0004-6361/202037583.

[40] Kóspál Á., Ábrahám P., Goto M., Regály Z., Dullemond C.P., Henning T., Juhász A., SiciliA-Aguilar A., and van den Ancker M. Near-infrared

spectroscopy of EX Lupi in outburst. *Astrophys. J.*, 736(1):72, 2011. doi:10.1088/0004-637X/736/1/72.

[41] Mantz A.W. and Maillard J.P. Emission spectra with a high resolution fourier transform spectrometer: CO spectra and their astrophysical importance. *J. Mol. Spectrosc.*, 53(3):466–478, 1974. doi:10.1016/0022-2852(74)90083-6.

[42] Tan Y., Wang J., Zhao X.Q., Liu A.W., and Hu S.M. Cavity ring-down spectroscopy of the fifth overtone of CO. *J. Quant. Spectrosc. Radiat. Transfer*, 187:274–279, 2017. doi:10.1016/j.jqsrt.2016.10.003.

[43] Medvedev E. and Ushakov V. Effect of the analytical form of the dipole-moment function on the rotational intensity distributions in the high-overtone vibrational bands of carbon monoxide. *J. Quant. Spectrosc. Radiat. Transfer*, 272:107803, 2021. doi:10.1016/j.jqsrt.2021.107803.

[44] Meshkov V., Ermilov A., Stolyarov A., Medvedev E., Ushakov V., and Gordon I. Semi-empirical dipole moment of carbon monoxide and line lists for all its isotopologues revisited. *J. Quant. Spectrosc. Radiat. Transfer*, 280:108090, 2022. doi:10.1016/j.jqsrt.2022.108090.

[45] Gordon I., Rothman L., Hargreaves R., Hashemi R., Karlovets E., Skinner F., Conway E., Hill C., Kochanov R., Tan Y., Wcisło P., Finenko A., Nelson K., Bernath P., Birk M., Boudon V., Campargue A., Chance K., Coustenis A., Drouin B., Flaud J.M., Gamache R., Hodges J., Jacquemart D., Mlawer E., Nikitin A., Perevalov V., Rotger M., Tennyson J., Toon G., Tran H., Tyuterev V., Adkins E., Baker A., Barbe A., Canè E., Császár A., Dudaryonok A., Egorov O., Fleisher A., Fleurbaey H., Foltynowicz A., Furtenbacher T., Harrison J.,

Hartmann J.M., Horneman V., Huang X., Karman T., Karns J., Kassi S., Kleiner I., Kofman V., Kwabia–Tchana F., Lavrentieva N., Lee T., Long D., Lukashevskaya A., Lyulin O., Makhnev V., Matt W., Massie S., Melosso M., Mikhailenko S., Mondelain D., Müller H., Naumenko O., Perrin A., Polyansky O., Raddaoui E., Raston P., Reed Z., Rey M., Richard C., Tóbiás R., Sadiek I., Schwenke D., Starikova E., Sung K., Tamassia F., Tashkun S., Auwera J.V., Vasilenko I., Vigasin A., Villanueva G., Vispoel B., Wagner G., Yachmenev A., and Yurchenko S. The hitran2020 molecular spectroscopic database. *J. Quant. Spectrosc. Radiat. Transfer*, 277:107949, 2022. doi:10.1016/j.jqsrt.2021.107949.

[46] O'Keefe A. and Deacon D.A.G. Cavity ring-down optical spectrometer for absorption measurements using pulsed laser sources. *Rev. Sci. Instrum.*, 59 (12):2544–2551, 1988. doi:10.1063/1.1139895.

[47] Kassi S., Gordon I.E., and Campargue A. First detection of transitions in the second quadrupole overtone band of nitrogen near 1.44 m by CW-CRDS with 6×10^{-13}cm^{-1} sensitivity. *Chem. Phys. Lett.*, 582:6–9, 2013. doi:10.1016/j.cplett.2013.07.031.

[48] Long D.A., Truong G.W., van Zee R.D., Plusquellic D.F., and Hodges J.T. Frequency-agile, rapid scanning spectroscopy: absorption sensitivity of 2 $\times$ 10^{-12} cm^{-1} hz$^{-1/2}$ with a tunable diode laser. *Appl. Phys. B*, 114:489 – 495, 2014. doi:10.1007/s00340-013-5548-5.

[49] Cygan A., Lisak D., Morzyński P., Bober M., Zawada M., Pazderski E., and Ciuryło R. Cavity mode-width spectroscopy with widely tunable ultra narrow laser. *Opt. Express*, 21(24):29744–29754, 2013. doi:10.1364/OE.21.029744.

[50] Li G., Gordon I., Rothman L., Tan Y., Hu S.M., Kassi S., Campargue A., and Medvedev E. Rovibrational line lists for nine isotopologues of the CO molecule in the $X^1\Sigma^+$ ground electronic state. *Astrophys. J. Suppl. Ser.*, 216:15, 2015. doi:10.1088/0 067-0 049/216/1/15.

[51] Lisak D., Masłowski P., Cygan A., Bielska K., Wójtewicz S., Piwiński M., Hodges J.T., Trawiński R.S., and Ciuryło R. Line shapes and intensities of self-broadened O_2 $b\ ^1\Sigma_g^+(\nu = 1) \leftarrow X\ ^3\Sigma_g^-(\nu = 0)$ band transitions measured by cavity ring-down spectroscopy. *Phys. Rev. A*, 81:042504, 2010. doi:10.1103/PhysRevA.81.042504.

[52] Domysławska J., Wójtewicz S., Masłowski P., Cygan A., Bielska K., Trawiński R.S., Ciuryło R., and Lisak D. A new approach to spectral line shapes of the weak oxygen transitions for atmospheric applications. *J. Quant. Spectrosc. Radiat. Transfer*, 169:111–121, 2016. doi:10.1016/j.jqsrt.2015.10.019.

[53] Hodges J.T., Layer H.P., Miller W.W., and Scace G.E. Frequency-stabilized single-mode cavity ring-down apparatus for high-resolution absorption spectroscopy. *Rev. Sci. Instrum.*, 75(4):849–863, 2004. doi:10.1063/1.1666984.

[54] Drever R.W.P., Hall J.L., Kowalski F.V., Hough J., Ford G.M., Munley A.J., and Ward H. Laser phase and frequency stabilization using an optical resonator. *Appl. Phys. B*, 31(2):97–105, 1983. doi:10.1007/BF00702605.

[55] Zhu M. and Hall J.L. Stabilization of optical phase/frequency of a laser system: application to a commercial dye laser with an external stabilizer. *J. Opt. Soc. Am. B*, 10(5):802–816, 1993. doi:10.1364/JOSAB.10.000802.

[56] Black E.D. An introduction to Pound–Drever–Hall laser frequency stabilization.

Am. J. Phys., 69(1):79–87, 2001. doi:10.1119/1.1286663.

[57] Cygan A. *Spektroskopia strat we wnęce z aktywną stabilizacją częstotliwości*. PhD thesis, Toruń, 2012. doctoral dissertation.

[58] Wójtewicz S., Cygan A., Domysławska J., Bielska K., Morzyński P., Masłowski P., Ciuryło R., and Lisak D. Response of an optical cavity to phase-controlled incomplete power switching of nearly resonant incident light. *Opt. Express*, 26 (5):5644–5654, 2018. doi:10.1364/OE.26.005644.

[59] Cygan A., Wójtewicz S., Kowzan G., Zaborowski M., Wcisło P., Nawrocki J., Krehlik P., Śliwczyński ., Lipiński M., Masłowski P., Ciuryło R., and Lisak D. Absolute molecular transition frequencies measured by three cavity-enhanced spectroscopy techniques. *J. Chem. Phys.*, 144(21), 2016. doi:10.1063/1.4952651.

[60] Jiang Z., Czubla A., Nawrocki J., Lewandowski W., and Arias E.F. Comparing a GPS time link calibration with an optical fibre self-calibration with 200 ps accuracy. *Metrologia*, 52(2):384, 2015. doi:10.1088/0026-1394/52/2/384.

[61] Morzyński P., Bober M., Bartoszek-Bober D., Nawrocki J., Krehlik P., Śliwczyński ., Lipiński M., Masłowski P., Cygan A., Dunst P., Garus M., Lisak D., Zachorowski J., Gawlik W., Radzewicz C., Ciuryło R., and Zawada M. Absolute measurement of the $^1S_0 - {}^3P_0$ clock transition in neutral ^{88}Sr over the 330 km-long stabilized fibre optic link. *Sci. Rep.*, 5, 2015. doi:10.1038/srep17495.

[62] Krehlik P., Łukasz Śliwczyński, Łukasz Buczek, Kołodziej J., and Lipiński M. Ultrastable long-distance fibre-optic time transfer: active compensation over a wide range of delays. *Metrologia*, 52(1):82, 2015. doi:10.1088/0026-1394/52/1/82.

[63] Bielska K., Domysławska J., Wójtewicz S., Balashov A., Slowiński M., Piwiński M., Cygan A., Ciuryło R., and Lisak D. Simultaneous observation of speed dependence and Dicke narrowing for self-perturbed P-branch lines of O_2 B band. *J. Quant. Spectrosc. Radiat. Transfer*, 276:107927, 2021. doi:10.1016/j.jqsrt.2021.107927.

[64] Brunt D. Notes on radiation in the atmosphere. I. *Q. J. R. Meteorol. Soc.*, 58 (247):389–420, 1932. doi:10.1002/qj.49705824704.

[65] Elsasser W.M. Far Infrared Absorption of Atmospheric Water Vapor. *Astrophys. J.*, 87:497, 1938. doi:10.1086/143940.

[66] Elsasser W.M. Note on atmospheric absorption caused by the rotational water band. *Phys. Rev.*, 53:768–768, 1938. doi:10.1103/PhysRev.53.768.

[67] van Vleck J.H. The absorption of microwaves by oxygen. *Phys. Rev.*, 71:413–424, 1947. doi:10.1103/PhysRev.71.413.

[68] Ptashnik I.V. and Rädel G. The water vapour continuum: Brief history and recent developments. *Surv. Geophys.*, 33:535–555, 2012. doi:10.1007/s10712-011-9170-y.

[69] Frommhold L. *Collision-induced Absorption in Gases*. Cambridge Monographs on Atomic, Molecular and Chemical Physics. Cambridge University Press, 1994. doi:10.1017/CBO9780511524523.

[70] Serov E.A., Balashov A.A., M. Yu. Tretyakov, Odintsova T.A., Koshelev M.A., Chistikov D.N., Finenko A.A., Lokshtanov S.E., Petrov S.V., and Vigasin A.A. Continuum absorption of millimeter waves in ni-

trogen. *J. Quant. Spectrosc. Radiat. Transfer*, 242:106774, 2020. doi:https://doi.org/10.1016/j.jqsrt.2019.106774.

[71] Odintsova T.A., Serov E.A., Balashov A.A., Koshelev M.A., Koroleva A.O., Simonova A.A., M. Yu. Tretyakov, Filippov N.N., Chistikov D.N., Finenko A.A., Lokshtanov S.E., Petrov S.V., and Vigasin A.A. CO_2–CO_2 and CO_2–Ar continua at millimeter wavelengths. *J. Quant. Spectrosc. Radiat. Transfer*, 258: 107400, 2021. doi:10.1016/j.jqsrt.2020.107400.

[72] Hartmann J.M., Boulet C., and Robert D. *Collisional effects on molecular spectra*. Elsevier, Amsterdam, second edition, 2021.

[73] Hartmann J.M., Tran H., Armante R., Boulet C., Campargue A., Forget F., Gianfrani L., Gordon I., Guerlet S., Gustafsson M., Hodges J.T., Kassi S., Lisak D., Thibault F., and Toon G.C. Recent advances in collisional effects on spectra of molecular gases and their practical consequences. *J. Quant. Spectrosc. Radiat. Transfer*, 213:178–227, 2018.

[74] Demtröder W. *Atoms, Molecules and Photons*. Graduate Texts in Physics, Molecular and Chemical Physics. Springer Berlin, Heidelberg, 2 edition, 2010. doi:10.1007/978-3-642-10298-1.

[75] Rohart F., Mäder H., and Nicolaisen H. Speed dependence of rotational relaxation induced by foreign gas collisions: Studies on CH_3F by millimeter wave coherent transients. *J. Chem. Phys.*, 101(8):6475–6486, 1994. doi:10.1063/1.468342.

[76] Berman P.R. Speed-dependent collisional width and shift parameters in spec-

tral profiles. *J. Quant. Spectrosc. Radiat. Transfer*, 12(9):1331–1342, 1972. doi:10.1016/0022-4073(72)90189-6.

[77] Dicke R.H. The effect of collisions upon the doppler width of spectral lines. *Phys. Rev.*, 89:472–473, 1953. doi:10.1103/PhysRev.89.472.

[78] Rautian S.G. and Sobel'man I.I. The effect of collisions on the doppler broadening of spectral lines. *Phys. Usp.*, 9(5):701–716, 1967. doi:10.1070/PU1967v009n05ABEH003212.

[79] Pine A.S. Line shape asymmetries in Ar-broadened HF(v=1–0) in the Dicke-narrowing regime. *J. Chem. Phys.*, 101(5):3444–3452, 1994. doi:10.1063/1.467529.

[80] Demeio L., Green S., and Monchick L. Effects of velocity changing collisions on line shapes of HF in Ar. *J. Chem. Phys.*, 102(23):9160–9166, 1995. doi:10.1063/1.468864.

[81] Thibault F., Patkowski K., Żuchowski P.S., Jóźwiak H., Ciuryło R., and Wcisło P. Rovibrational line-shape parameters for H_2 in He and new H_2-He potential energy surface. *J. Quant. Spectrosc. Radiat. Transfer*, 202:308–320, 2017. doi:10.1016/j.jqsrt.2017.08.014.

[82] Lindenfeld M.J. Self-structure factor of hard-sphere gases for arbitrary ratio of bath to test particle masses. *J. Chem. Phys.*, 73(11):5817–5829, 2008. doi:10.1063/1.440066.

[83] Galatry L. Simultaneous effect of doppler and foreign gas broadening on spectral lines. *Phys. Rev.*, 122:1218–1223, 1961. doi:10.1103/PhysRev.122.1218.

[84] Nelkin M. and Ghatak A. Simple binary collision model for Van Hove's $G_s(r,t)$. *Phys. Rev.*, 135:A4–A9, 1964. doi:10.1103/PhysRev.135.A4.

[85] Ngo N., Lisak D., Tran H., and Hartmann J.M. An isolated line-shape model to go beyond the Voigt profile in spectroscopic databases and radiative transfer codes. *J. Quant. Spectrosc. Radiat. Transfer*, 129:89–100, 2013. doi:10.1016/j.jqsrt.2013.05.034.

[86] Tennyson J., Bernath P.F., Campargue A., Császár A.G., Daumont L., Gamache R.R., Hodges J.T., Lisak D., Naumenko O.V., Rothman L.S., Tran H., Zobov N.F., Buldyreva J., Boone C.D., Vizia M.D.D., Gianfrani L., Hartmann J.M., McPheat R., Weidmann D., Murray J., Ngo N.H., and Polyansky O.L. Recommended isolated-line profile for representing high-resolution spectroscopic transitions (IUPAC technical report). *Pure Appl. Chem.*, 86(12): 1931–1943, 2014. doi:doi:10.1515/pac-2014-0208.

[87] Ngo N., Lin H., Hodges J., and Tran H. Spectral shapes of rovibrational lines of co broadened by He, Ar, Kr and SF_6: A test case of the Hartmann-Tran profile. *J. Quant. Spectrosc. Radiat. Transfer*, 203:325–333, 2017. doi:10.1016/j.jqsrt.2017.03.001. HITRAN2016 Special Issue.

[88] Baranger M. Problem of overlapping lines in the theory of pressure broadening. *Phys. Rev.*, 111:494–504, 1958. doi:10.1103/PhysRev.111.494.

[89] Rosenkranz P. Shape of the 5 mm oxygen band in the atmosphere. *IEEE Trans. Antennas Propag.*, 23(4):498–506, 1975. doi:10.1109/TAP.1975.1141119.

[90] Šimečková M., Jacquemart D., Rothman L.S., Gamache R.R., and Goldman A. Einstein A-coefficients and statistical weights for molecular absorption tran-

sitions in the hitran database. *J. Quant. Spectrosc. Radiat. Transfer*, 98(1): 130–155, 2006. doi:https://doi.org/10.1016/j.jqsrt.2005.07.003.

[91] Marquardt D.W. An algorithm for least-squares estimation of nonlinear parameters. *SIAM J. Appl. Math.*, 11(2):431–441, 1963. doi:10.1137/0111030.

[92] Ciuryło R. and Pine A. Speed-dependent line mixing profiles. *J. Quant. Spectrosc. Radiat. Transfer*, 67(5):375–393, 2000. doi:10.1016/S0022-4073(00)00030-3.

[93] Benner D., Rinsland C.P., Devi V., Smith M.A.H., and Atkins D. A multispectrum nonlinear least squares fitting technique. *J. Quant. Spectrosc. Radiat. Transfer*, 53(6):705–721, 1995. doi:10.1016/0022-4073(95)00015-D.

[94] Pine A. and Ciurylo R. Multispectrum fits of Ar-broadened HF with a generalized asymmetric lineshape: Effects of correlation, hardness, speed dependence, and collision duration. *J. Mol. Spectrosc.*, 208(2):180–187, 2001. doi:10.1006/jmsp.2001.8375.

[95] Boulet C., Flaud P.M., and Hartmann J.M. Infrared line collisional parameters of HCl in argon, beyond the impact approximation: Measurements and classical path calculations. *J. Chem. Phys.*, 120(23):11053–11061, 2004. doi:10.1063/1.1714794.

[96] Reed Z.D., Tran H., Ngo H.N., Hartmann J.M., and Hodges J.T. Effect of non-markovian collisions on measured integrated line shapes of co. *Phys. Rev. Lett.*, 130:143001, 2023. doi:10.1103/PhysRevLett.130.143001.

[97] Cygan A., Lisak D., Wójtewicz S., Domysławska J., Hodges J.T., Trawiński

R.S., and Ciuryło R. High-signal-to-noise-ratio laser technique for accurate measurements of spectral line parameters. *Phys. Rev. A*, 85:022508, 2012. doi:10.1103/PhysRevA.85.022508.

[98] Bui T.Q., Long D.A., Cygan A., Sironneau V.T., Hogan D.W., Rupasinghe P.M., Ciuryło R., Lisak D., and Okumura M. Observations of Dicke narrowing and speed dependence in air-broadened CO2 lineshapes near 2.06 m. *J. Chem. Phys.*, 141(17), 2014. doi:10.1063/1.4900502.

[99] Fox R.W. and Hollberg L. Role of spurious reflections in ring-down spectroscopy. *Opt. Lett.*, 27(20):1833–1835, 2002. doi:10.1364/OL.27.001833.

[100] Courtois J. and Hodges J.T. Coupled-cavity ring-down spectroscopy technique. *Opt. Lett.*, 37(16):3354–3356, 2012. doi:10.1364/OL.37.003354.

[101] Bell S. *Measurement Good Practice Guide No. 11*, volume 11, chapter 7.1.2, page 13. National Physical Laboratory, Teddington, Middlesex, United Kingdom, TW11 0LW, issue 2 edition, 2001.

[102] Hashemi R., Gordon I., Adkins E., Hodges J., Long D., Birk M., Loos J., Boone C., Fleisher A., Predoi-Cross A., and Rothman L. Improvement of the spectroscopic parameters of the air- and self-broadened N_2O and CO lines for the HITRAN2020 database applications. *J. Quant. Spectrosc. Radiat. Transfer*, 271:107735, 2021. doi:10.1016/j.jqsrt.2021.107735.

[103] Coxon J. and Hajigeorgio P. Direct potential fit analysis of the $X^1\Sigma^+$ ground state of CO. *J. Chem. Phys.*, 121:2992, 2004. doi:10.1063/1.1768167.

[104] Medvedev E.S. and Ushakov V.G. Irregular semi-empirical dipole-moment func-

tion for carbon monoxide and line lists for all its isotopologues verified for extremely high overtone transitions. *J. Quant. Spectrosc. Radiat. Transfer*, 288: 108–255, 2022. doi:10.1016/j.jqsrt.2022.108255.

[105] Bielska K., Kyuberis A., Reed Z., Li G., Cygan A., Ciuryło R., Adkins E., Lodi L., Zobov N., Ebert V., Lisak D., Hodges J., Tennyson J., and Polyansky O. Subpromille Measurements and Calculations of CO (3–0) Overtone Line Intensities. *Phys. Rev. Lett.*, 129:043002, 2022. doi:10.1103/PhysRevLett.129.043002.

[106] Balashov A., Bielska K., Li G., Kyuberis A., Wójtewicz S., Domysławska J., Ciuryło R., Zobov N., Lisak D., J.Tennyson, and Polyansky. O. Measurement and calculation of CO (7-0) overtone line intensities. *J. Chem. Phys.*, 2023. doi:10.1063/5.0152996. Accepted in volume 158.

[107] Cygan A., Wcisło P., Wójtewicz S., Masłowski P., Hodges J.T., Ciuryło R., and Lisak D. One-dimensional frequency-based spectroscopy. *Opt. Express*, 23(11): 14472–14486, 2015. doi:10.1364/OE.23.014472.

[108] Bielska K., Tran D., Balashov A., Domyslawska J., Wójtewicz S., Bober M., Bilicki S., Ciuryło R., and Lisak D. Pressure and temperature dependencies of air-perturbed O_2 B-band line shapes. *Spectrochim. Acta A*, 2023. submitted.

[109] Ciuryło R. Shapes of pressure- and Doppler-broadened spectral lines in the core and near wings. *Phys. Rev. A*, 58:1029–1039, 1998. doi:10.1103/PhysRevA.58.1029.